Development and Performance of a Screw-Propelled ISRU Excavation System

by

Marko Green

A Thesis Presented in Partial Fulfillment
of the Requirements for the Degree
Master of Science

Approved July 2021 by the
Graduate Supervisory Committee:

Hamidreza Marvi, Chair
Heather Emady
Hyunglae Lee

ARIZONA STATE UNIVERSITY

August 2021

ABSTRACT

Regolith excavation systems are the enabling technology that must be developed in order to implement many of the plans for in-situ resource utilization (ISRU) that have been developed in recent years to aid in creating a lasting human presence on the surface of the Moon, Mars, and other celestial bodies. The majority of proposed ISRU excavation systems are integrated onto a wheeled mobility system, however none yet have proposed the use of a screw-propelled vehicle, which has the potential to augment and enhance the capabilities of the excavation system. As a result, CASPER, a novel screw-propelled excavation rover is developed and analyzed to determine its effectiveness as a ISRU excavation system. The excavation rate, power, velocity, cost of transport, and a new parameter, excavation transport rate, are analyzed for various configurations of the vehicle through mobility and excavation tests performed in silica sand. The optimal configuration yielded a 28.4 kg/hr excavation rate and 11.2 m/min traverse rate with an overall system mass of 3.4 kg and power draw of 26.3 W. CASPER's mobility and excavation performance results are compared to four notable proposed ISRU excavation systems of various types. The results indicate that this architecture shows promise as an ISRU excavator because it provides significant excavation capability with low mass and power requirements.

DEDICATION

This thesis is dedicated to the love of my life, Caitlyn, my parents, Brian and Erika,

and my many friends and relatives whose ceaseless and vigorous support over the

years has been instrumental to the completion of this research.

ACKNOWLEDGMENTS

TABLE OF CONTENTS

LIST OF TABLES

LIST OF FIGURES

Chapter 1

INTRODUCTION

1.1   Motivation for ISRU Excavation

The exploration of the celestial bodies in the solar system has been one of the most meaningful pursuits undertaken in the history of human civilization. Learning about our neighboring worlds has been a fruitful source of scientific discovery, leading to new insights across many fields such as planetary geology, cosmology, climate science, biology, and astrophysics, just to name a few. Furthermore, space exploration has inspired the development of critical technologies including water purifiers, smoke detectors, cell phone cameras, GPS, and countless other devices and processes. These technological developments have cascaded through society and raised the standard of living for billions of people worldwide. Not only does space exploration provide scientific discoveries and a forcing function for the advancement of technology, but it also provides the path forward into a sustainable future for the human species. It is in humanities best interest to expand out into solar system because it will greatly expand our resource base, develop our ability to defend ourselves from potential impact events, and will continue to inspire people young and old to appreciate and get involved in the STEM fields, which will be critical to our ability to solve great problems facing humanity in the future.

One of the most promising methods for enabling human exploration of nearby planetary bodies is in-situ resource utilization (ISRU). The premise of ISRU is to extract and process local raw materials, and use them to produce resources that enable

or sustain surface exploration of that celestial body. Some of the most near term ISRU goals would be mining water ice deposits that can be found in the permanently shadowed craters of the moon, or in the near subsurface of the northern latitudes of Mars. This water ice could be used to produced many vital resources for supporting a sustained human presence. Primarily, the ice could be melted to provide liquid water for drinking and sanitation. It could also be electrolyzed to produce oxygen for breathing. Arguably the most important ISRU application for water ice is producing hydrogen and oxygen to be used as fuel and oxidizer for rocket engines. Production of in-situ rocket propellant is a paradigm shift for mission design. If you can produce your return propellant at the target destination, the payload you can bring with you on the outbound journey increases dramatically, enabling larger and safer spacecraft to reach the surface.

Before any of the lofty goals of ISRU can be realized, the basic methods of efficiently extracting the raw materials must be created and mastered. In order to extract the raw materials, a robotic system comprising of a mobility system for traversing the local surface and an excavation system for extracting material must be developed.

The mobility system must be capable of locomotion on the surface of celestial bodies that are covered in regolith, which is made up primarily of granular media and rocks. Achieving mobility on planetary surfaces is not as easy as it is on the Earth, primarily due to the fact that all solid celestial bodies in the solar system have a lower gravitational acceleration than the Earth. This leads to a lower weight for a given mass, which reduces the amount of traction force that a given mobility system is able to generate. Many different techniques of locomotion on planetary surfaces have been researched an implemented, and they will be examined in depth in the next section.

The excavation system must be capable of extracting material from the surface

and storing it until it can be deposited at a processing station. Excavation on celestial bodies is more complicated than on the Earth for similar reasons as mobility. For most bodies, the regolith is likely going to be quite compacted after being compressed by gravity for a great deal of time, which means that it will take a significant amount of force to penetrate the surface and remove material. This implies that the robotic craft as a whole must generate enough force through its weight and traction to react against the excavation system and enable the extraction of material from the surface. Unfortunately, as described earlier, the lower gravity causes the robot to weigh less and produce less traction. Many different techniques have been researched and tested for excavation in a space environment, and the benefits and drawbacks of each of these will be discussed in depth in the following sections.

1.2   Planetary Mobility Systems

1.2.1   Apollo Lunar Roving Vehicle (LRV)

There are many methods of enabling surface mobility on celestial bodies that have been researched and implemented since the inception of this field in the middle of the twentieth century. One of the first practical systems for mobility on the lunar surface was the Apollo program's Lunar Roving Vehicle (LRV), which was used to expand the exploration capability of the Apollo 15-17 missions. An image of the LRV in operation is shown in Figure 1 [1].

The LRV utilized a wheeled mobility system that was driven by four battery powered electric motors [2]. The rover was designed to safely and reliably ferry crew and cargo across the lunar surface at a top speed between 9 - 13 km/h [2]. Additionally,

3
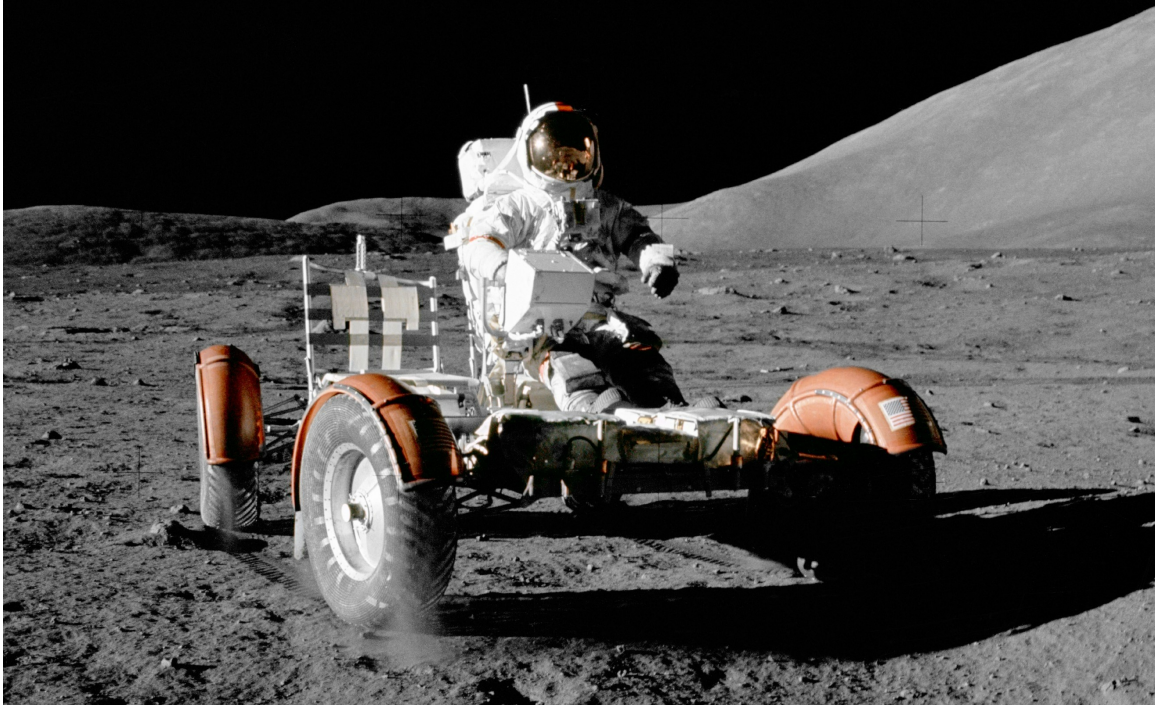
Figure 1. Apollo Lunar Roving Vehicle (LRV) on the Lunar Surface.

the rover was required be capable able of traversing slopes of 25° while being subjected to lunar gravity [3], which is approximately 1/6 of the gravity experienced on Earth. The wheels themselves were comprised of a mesh of woven steel wire surrounding an aluminum hub [4]. Additionally, the wheels had chevron shaped tread features which were made of titanium and riveted to the mesh to increase traction and durability. While the LRV mobility system was successful, the rover architectures that followed the LRV opted for different types of wheels and mobility subsystems.

1.2.2 Mars Rovers: Sojourner, MER, and MSL

After the Apollo program ended, the focus of NASA's space exploration pivoted to focus on robotic exploration of celestial bodies, namely, Mars. Since then, the NASA

Jet Propulsion Laboratory has designed and developed three generations of roving science platforms: the Sojourner rover, the Mars Exploration Rovers (MER) Spirit and Opportunity, and the Mars Science Laboratory (MSL) Curiosity. These rovers and a detailed view of their wheels are shown in Figure 2 [5, 6].
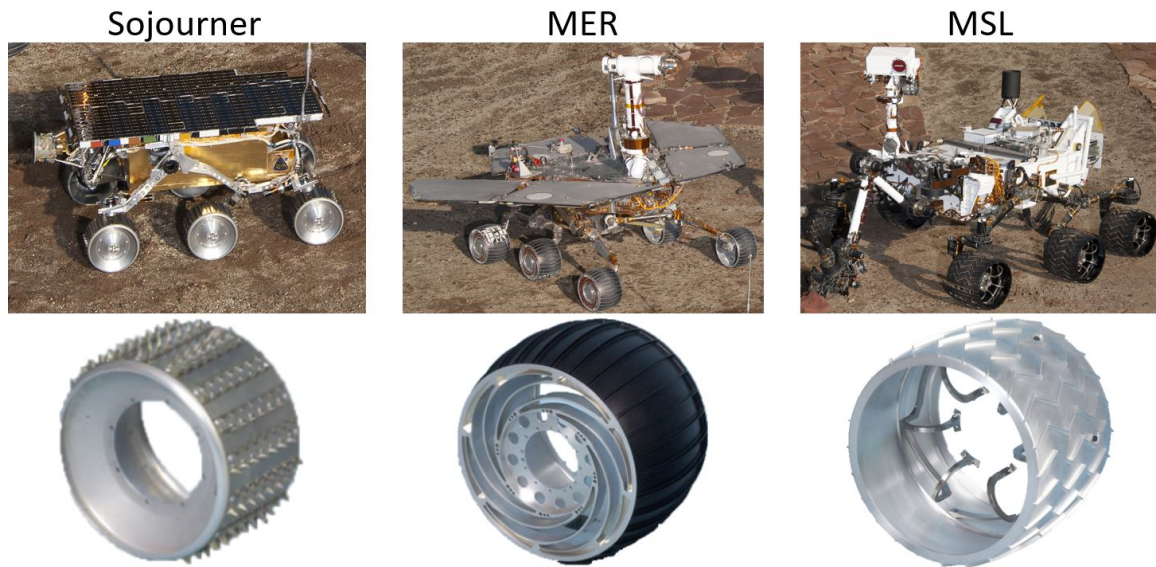
Figure 2. Sojourner, MER, and MSL Rovers and Their Wheels.

In the late 1990s, the Sojourner rover was developed as a secondary payload for the Pathfinder lander. This rover was small with a mass of only 11.5 kg [7], but it pioneered many mobility system methods that have been featured on all Mars rovers that have followed in its footsteps, such as a mobility system with six wheels, and a rocker-bogie suspension. All six wheels were driven by electric motors, with only the four corner wheels being capable of turning [7]. Figure 2 shows that the Sojourner wheels have tread features comprised of rows of linear spikes evenly spaced around the rim. These tread features are dramatically different than the riveted chevron features found on the LRV wheels. The rocker-bogie suspension is designed to rotate the wheel linkages on one side of the rover about a differential in the center of the rover body in

response to obstacles or changes in terrain [8]. This rocking motion leads to minimal motion of the rover body during obstacle traversal, and ensures that all 6 wheels remain in contact with the surface at all times. These features are highly desirable, and expand the operational envelope of planetary rovers, which is why they have been features on all of NASA's Mars rovers. Sojourner was solar-powered, and as a result, Martian dust eventually covered the solar panels causing the rover to cease operations after 83 days [7]. Despite the fact that Sojourner was relatively short-lived, it paved the way for the Mars Exploration Rovers Spirit and Opportunity that came after it.

Following the success of the Sojourner rover, NASA developed two Mars Exploration Rovers: Spirit and Opportunity. The MER rovers were more than an order of magnitude more massive than Sojourner with a total mass of 176.5 kg [9]. This allowed for the MER rovers to carry much more sophisticated scientific instruments, however, they still utilized the six-wheeled rocker-bogie mobility system that was flight-proven on Sojourner. Just like Sojourner, all six wheels were driven by DC motors, with only the four corner wheels being equipped with motorized turning systems [9]. While the base concept of the mobility system was the same, several improvements were made, the most notable and relevant to this work being the addition of grousers to the wheel. Grousers are typically short paddle-like features that extrude radially outward from the surface of the rim of a wheel. They improve the performance of the wheel by increasing the thrust generated and reducing the likelihood of slip on flat and sloped surfaces. One might think that the grousers themselves produce additional thrust, however this is not the case. Studies on the mechanisms that cause this increased performance from grousers [10, 11] indicate that the grousers induce shearing motion in the soil prior to the rim surface making contact. This shearing motion compacts the soil which reduces compaction resistance on the

wheel. The overall effect is increased thrust and reduced slip risk, which is highly desirable for planetary rovers, and is the reason that grousers have been featured on all of NASA's rover wheels in the 21st century.

Before the MER missions had concluded, NASA designed and developed its next generation rover, the Mars Science Laboratory Curiosity, which landed on Mars in 2011. Weighing in at 900 kg [12], MSL was much larger than the MER rovers and Sojourners. Despite the increase in mass, it also made use of a six-wheeled rocker-bogie mobility system, but the wheel design featured major changes from MER. Due to the sky-crane landing method, the MSL wheels had to act as landing gear as well as wheels. To achieve this, the rim was fixed to the central hub using flexures that allowed the wheel to elastically deform and safely absorb the shock of landing [13]. Another deviation from the MER wheel design was the chevron grouser tread pattern. The change from straight grousers to chevron grousers improved the ability of the mobility system to handle traverses across slopes without slipping [13].

Although planetary rovers have had immense success using wheeled mobility systems, there are some features of wheels that could pose problems on an ISRU excavation system. There is a limit to the amount of tractive thrust force that can be generated before the wheel slips. This problem is increasingly more prevalent the lower the gravitational acceleration becomes. Additionally, research indicates that forces required to excavate regolith can be significantly large [14]. This insight, coupled with the low weight and traction forces experienced on planetary surfaces imply that an ISRU excavator should maximize the amount of traction provided by the mobility system and minimize the excavation force in order to enable efficient excavation for ISRU [15]. Although grousers have been shown to increase the tractive force, wheels are still limited in comparison to other types of mobility systems such as tracks or

screws. The type of mobility system an ISRU excavator is based upon is critical, and this thesis will seek to demonstrate the benefits a screw propulsion system has on excavation performance.

1.3 ISRU Excavation Systems

Research dictates that there are two primary families of excavation systems which each have unique advantages: discrete and continuous [16]. Note that there are many instances of excavation systems which are not integrated onto a mobility platform, known as partial systems [16]. Conversely, an excavation system that is integrated with a mobility system is referred to as a complete system [16]. Since the focus of this work is the development of complete excavation system, an overview of partial systems will not be provided. The following subsections will explain the distinction between discrete and continuous excavation, and will provide examples of complete systems of each type being developed for ISRU on planetary bodies.

1.3.1 Discrete Excavation Systems

A discrete excavator is a platform which removes material from the target location in individual cuts [16]. Furthermore, after each cut, the collection device must break contact with the target location in order to deposit the excavated material. After the material is deposited, the discrete collection cycle is complete, and the excavator must repeatedly execute this process to keep collecting material.

There are many examples of discrete excavation systems utilized in industrial construction, such as backhoes or front-end loaders that one might see on a construction

site. These excavators require massive reaction forces because they remove a large amount of material with each cut. Furthermore, they are typically implemented on track mobility systems. While track-based systems are highly effective on Earth, the tracks themselves induce a significant amount friction [17], which makes tracks less efficient than other types of mobility systems, and suboptimal for a power-limited space vehicle.

Figure 3. NASA Cratos Discrete Scraper Excavation Vehicle Depositing Lunar Regolith Simulant.

Another sub-type of discrete excavator, the scraper, has shown promise as a planetary ISRU excavator. In the hopes of developing a small vehicle capable of enabling lunar ISRU, NASA developed the Cratos robotic vehicle [18]. As shown in Figure 3 [19], Cratos features an actuated scraper bin which is capable of collecting material, storing it during transit, and depositing it at a desired location. This excavation system is integrated with a track mobility system which enables Cratos to move freely over lunar regolith simulant. The development of this vehicle has indicated that smaller ISRU platforms like Cratos are capable of completing planetary ISRU objectives at low cost and with low risk of failure [18]. A quantitative performance

comparison between Cratos the CASPER ISRU excavation system developed in this work is provided in Chapter 4.

Until now, there has not been any research done on the performance of discrete scooper excavation systems [16]. A scooper distinguishes itself from scrapers by scooping up a small amount of material per cut, rather than digging in and scraping up a large quantity of material. While initially thought to be ineffective for planetary excavation, this work seeks to study the performance of a ramp-based discrete scooper excavation system augmented by an Archimedes screw-propelled mobility system.

1.3.2   Continuous Excavation Systems

The other primary type of excavation systems examined here are continuous excavation systems. A continuous excavation system uses many cutting surfaces that successively make contact with the regolith [16]. The collection cycle begins with one cutting surface making contact with the ground and collecting regolith. Then, as the first surface moves to store the collected sample, the second cutting surface follows the first one and begins its own cut. This process continuously occurs such that there is always one cutting surface excavating material, while the others are either storing the material or returning to make another cut. Research has shown that continuous excavation systems provide better performance for lightweight planetary excavators than their discrete counterparts [20]. The reason for this is because continuous excavators encounter fresh, lightly compacted soil for each, and do not suffer from the build-up of resistance from material accumulation like scrapers do.

Two of the most successful continuous excavator subtypes are the bucket drum and the bucket wheel. NASA's RASSOR prototype [21] is an example of a bucket

Figure 4. NASA RASSOR Bucket Drum Continuous Excavation Vehicle Operating in Lunar Regolith Simulant.

drum excavator with a wheeled mobility system and it is shown in Figure 4 [22]. The system consists of two rotating drums mounted on actuating arms that extend from the central chassis of the robot where the wheels are mounted. Each drum features many circumferential scoop-like protuberances that collect material and deposit it into the drum itself as it rotates. RASSOR is unique because its dual bucket drums can be engaged simultaneously and rotate in opposite directions, which provides the reaction force needed for excavation without relying on weight or traction.

A bucket wheel system operates on a similar principal, where a circular formation of buckets is rotated such that each bucket makes contact with the soil at the bottom and deposits the material into a collection bin before its next cut [23, 24]. This type of system was mounted on the Scarab [25] and the Polaris [23, 24] mobility platforms such that the bucket wheel made cuts perpendicular to the direction of travel. The performance of the bucket wheel on these two systems will be compared to the CASPER prototype in Chapter 4.

1.4 Screw-Propelled Vehicles

Screwed-Propelled Vehicles (SPVs) are mobility platforms that use rotating pontoons with helical protuberances to generate thrust. These helical pontoons partially burrow into and displace the media which pushes the vehicle forward. SPVs are rarely used, both in terrestrial and planetary applications. Despite their rarity, SPVs are capable of traversing terrains that are simply impossible for wheeled and track-based mobility systems. Several examples where SPVs have had success include amphibious settings, arctic environments, or where clay or marshes are present [26, 27, 28]. SPVs are able to succeed in these harsh conditions due to several key characteristics: mechanical simplicity, large surface area for traction, and ability to function in both dry and wet conditions. The Russian ZIL-2906, pictured in Figure 5 [29], was a screw-propelled recovery vehicle designed to rapidly traverse the Siberian tundra to search for cosmonauts immediately after landing from orbit.

Figure 5. The ZIL-2906, a Screw-Propelled Russian Cosmonaut Recovery Vehicle.

Based on the success of SPVs in extreme environments, researchers began investigating their effectiveness in traversing granular media and their potential applications in space environments. Experimental and computational investigations into the forces generated by screws in granular media [30, 31] have shown that screws are able to provide high thrust forces in sand and lunar regolith simulants. Additionally, screw-propelled mobility systems have been developed and tested in the lunar regolith analogue BP-1. The development and evolution of this mobility platform is detailed in Chapter 3. Furthermore, the performance of this system has been computationally tested using gravity variant coupled discrete element method and multi-body dynamics simulations[32, 33, 34, 35]. Results indicate that screw propelled vehicles work well across a wide range of gravities. In addition, scaling laws have been developed that relate craft size parameters and the ambient gravitational acceleration to the craft's velocity and power draw [32, 33, 34, 35]. These scaling laws can be used to predict the performance of a prototype on a celestial body such as the moon or Mars by scaling measured performance values from experiments on Earth. Building upon this prior body of work, a screw-propelled excavation rover was developed and serves as the primary focus of this thesis. This vehicle aims to meet the requirements of in-space excavation by using the screw propulsion system to provide high tractive force and reduce the excavation force by taking advantage of the fact that the screws churn the granular media and reduce its compaction.

1.5   Organization of this Thesis

The work presented in this thesis is organized into five chapters. **Chapter 1** provides the motivation for the development of an ISRU excavation system, summarizes

the traditional methods of mobility on planetary surfaces, gives an overview of the various excavation methods being researched, introduces screw-propelled vehicles (SPV), and describes the benefits an SPV has as an ISRU excavation system. **Chapter 2** introduces and detail the design of the CASPER prototype vehicle, as well as introducing the general experimental equipment and methods used to analyze the performance of the vehicle developed and studied for this work. **Chapter 3** details the experimental investigation into CASPER's performance as an ISRU excavation vehicle, and presents and analyzes the results. **Chapter 4** compares CASPER's performance to various other excavation vehicles found in the scientific literature. **Chapter 5** presents the overall conclusions drawn from the entirety of this body of work, and provide potential avenues for future research.

Chapter 2

CASPER: COUNTER-ROTATING ARCHIMEDES SCREW PROPELLED EXCAVATION ROVER

2.1 Overview

The CASPER prototype was developed and tested to determine whether a screw-propelled discrete scooper excavation system might have some promise as a planetary ISRU excavator. It was also of interest to determine what excavation performance benefit the screw-propulsion system, especially with regards to the power consumption and excavation rate. An isometric view of the CASPER prototype is shown in Figure 6 and the dimensions of the vehicle are detailed in Table 1.
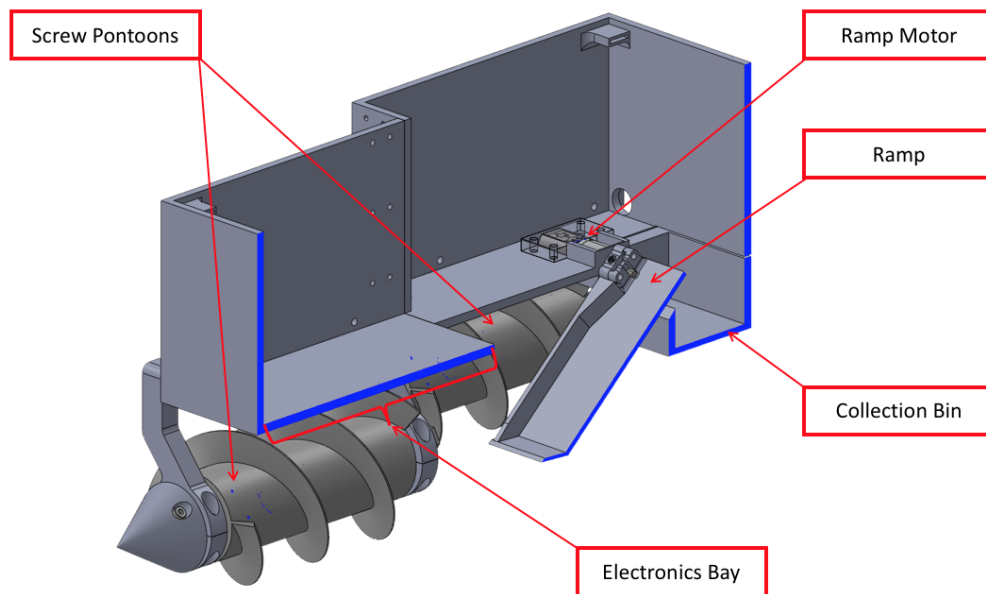
Figure 6. Isometric Section View of CASPER with Key Features Labeled.

Table 1. Dimensions of CASPER Vehicle

Subsystem	Parameter	Value
Body	Length	40 cm
	Width (front)	12.5 cm
	Width (rear)	20 cm
	Height	22.5 cm
	Total vehicle mass	3.35 kg
Pontoon	Length	20 cm
	Radius (center cylinder)	5 cm
	Radius (screw blade)	8 cm
Ramp	Length	13.5 cm
	Width	6.5 cm
	Tip angle	45°

The CASPER prototype was designed in Solidworks and the majority of the parts were printed in PETG with an FDM 3D printer. The body of the craft was printed in two parts and joined together with metal brackets and fasteners. All non-printed parts, including electronics components, bearings, motors, and fasteners were commercially sourced, most notably from McMaster-Carr, Grainger, Pololu, and Adafruit. The mobility system consists of four counter-rotating Archimedes screw pontoons, with the front two being mounted closer to the center line of the vehicle than the rear two. This layout causes the material churned by the front screws to be deposited in a wake that piles up towards the center of the vehicle, directly in line with the excavation ramp which sits between the two rear pontoons. The excavation system acts as a discrete scooper by using an actuated ramp to make a short, discrete cut from the central wake. Once collected, the ramp motor rotates the ramp into a vertical position such that the excavated material falls into the removable collection bin directly behind the ramp, concluding one excavation cycle. This process is repeated continuously as the vehicle traverses forward. Note that the rear pontoons eject the churned material outward, away from the center of the craft, and thus are purely for the purpose of mobility. Conversely, the front screws are used for mobility as well as augmenting the

excavation system by churning up the consolidated media prior to ramp collection. The design of CASPER's screw mobility system, ramp excavation system, electronics, and control scheme are detailed in the following section.

2.2 Design and Development

2.2.1 Helical Mobility System Design

The Archimedes screw-based mobility platform was initially developed for prior research into gravity variant granular scaling laws for screw-propelled and wheeled vehicles[33, 32, 34]. For that work, an experimental test craft was developed that utilized only two screw pontoons. While that first craft was successful in gathering data, it was not practically useful for excavation. The CASPER prototype makes use of four screw pontoons, each with an identical power train. An exploded view of the screw pontoon internals is shown in Figure 7.

Each pontoon is powered by a 12 V Pololu DC gear motor with a gear ratio of 75:1. The motors are equipped with a magnetic rotary encoder which enables the craft to determine its rotational position and velocity. The motor fits snug inside the motor sleeve, and is held flush against the base with two small screws on the forward end. On the forward side of the motor sleeve, the motor coupling attaches to the exposed motor shaft via a screw in the coupling that clamps onto the d-shaft of the motor. Next, the motor wires are fed through the hollow tube of the motor sleeve cap before the motor sleeve and the cap are seated together and sealed with a layer of strong tape around the joint. Once the motor sleeve assembly is complete, the rear bearing sleeve is pressure fitted onto the rear collar bearing. This collar bearing slides

17
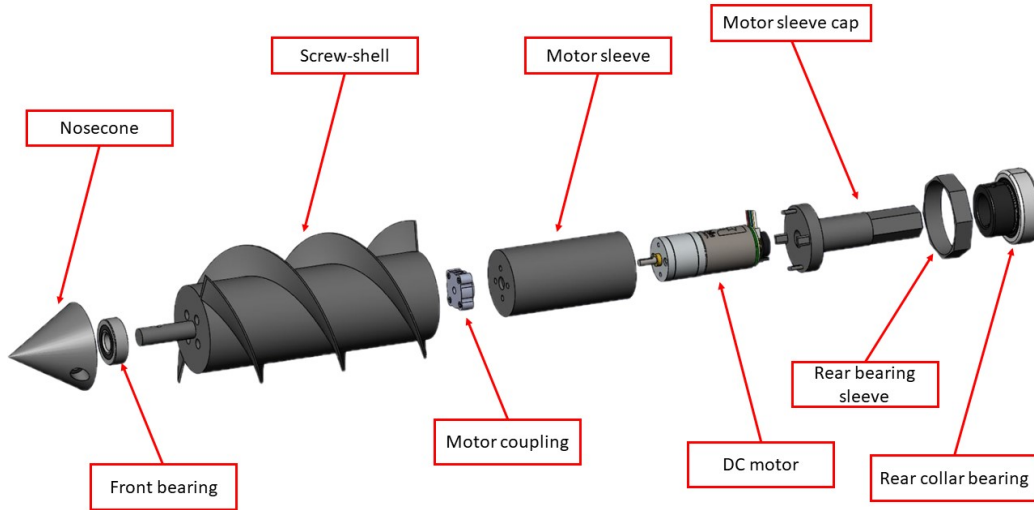
Figure 7. Exploded View of Screw Pontoons with Key Features Labeled.

onto the shaft of the end of the motor sleeve cap and is fixed in place with a set screw. This entire assembly slides into the screw shell, and is bolted in place through the front end of the screw shell, similar to how a car wheel is bolted to the wheel hub using lug nuts. Finally, the front bearing is slid onto the cylinder protruding from the front of the screw shell, and then the nosecone is attached to the same cylinder with a large bolt.

The octagonal pattern of the rear bearing sleeve locks in with the rear rim of the screw shell (not shown) to guarantee the motor torque causes the screw shell to rotate about the rear collar bearing. Similarly, the hexagonal pattern on the aft end of the motor sleeve cap locks into the pontoon mount that holds the pontoon in place with respect to the craft body. The other end of the mount has a circular cut-out that slides over the front bearing. Due to this setup, the pontoon is supported on the front end with a bearing, and the aft end is clamped. When the motor is activated, it reacts

against the pontoon mounts which hold it in place, and the torque is transferred to the screw shell which rotates about the front and rear bearings.

Special care was taken to prevent sand ingress into the internals of the screw-pontoons. The aft end of the screw shell and the rear bearing sleeve were printed at a slightly larger scale such that the material had to be sanded away from these parts prior to them fitting together. This tight pressure fit has proven to be effective in keeping sand and other debris out of the internal cavity. As mentioned previously, the joint between the motor sleeve and its associated cap is sealed with a layer of tape. Not only does this strengthen the joint, but it provides a second layer of protection for the motor and its wires. The end of the motor sleeve cap where the wires exit the pontoon was sealed with hot glue to prevent wire torsion and sand ingress. Combined, these measures have prevented any significant sand ingress during several thousand data collection runs through silica sand and BP-1.

2.2.2   Excavation System Design

CASPER's excavation system is comprised of two subsystems: the front screw pontoons and the ramp excavation system (pictured in Figure 8).

With the proper screw handedness and rotational direction, the front screws churn the granular media inwards, towards the center line of the vehicle. This creates an elevated wake of loosely compacted material behind the path of travel of the front pontoons. By design, this elevated wake is directly in front of the ramp excavation system. Powered by a Pololu 488:1 DC gear motor, the ramp withstands the drag force of the oncoming material for a specified load time prior to rotating the ramp into a vertical position. This rotation deposits the excavated material into the collection bin.

19
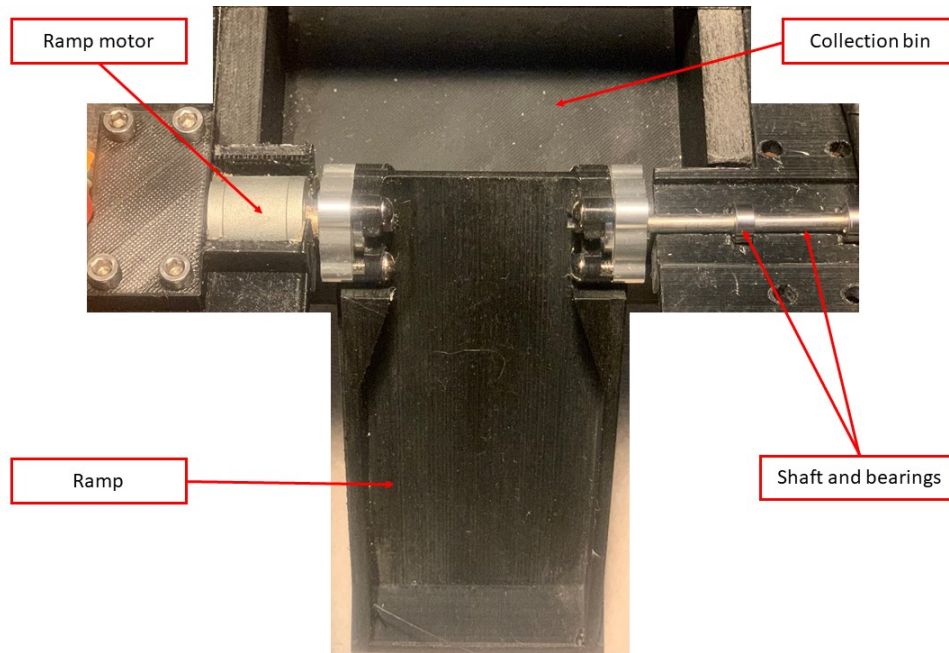
Figure 8. Ramp Excavation System with Key Features Labeled.

Note that this extremely high gear ratio was determined to be necessary to withstand the drag force of the ramp moving forward through the granular media through experimental testing. Lower gear ratio motors, such as stepper motors, were initially attempted. Unfortunately, these weaker options were incapable of withstanding the drag force produced by the forward motion of the ramp interacting with granular media. Ultimately, the high gear ratio DC motors were determined to be the best option, and are thus featured in the final design.

The ramp excavation system is made of several key components. The ramp gear motor provides both the reaction force during collection, and the torque to rotate the ramp to deposit material into the collection bin. An aluminum shaft supported by two bearings is seated opposite the ramp motor to guarantee smooth axial rotation of the ramp during operation. Both the ramp motor and the supporting aluminum shaft are affixed to the ramp via two d-shaft motor couplings which were attached

to the 3D printed ramp via bolts. The collection bin is a removable 3D printed part which is capable of holding over 250 grams of Quikrete silica sand before needing to be emptied. While this collection bin was sufficient to characterize the performance of the CASPER prototype, significant changes would need to be made to the collection bin to create a serviceable ISRU excavation system.

2.2.3 Electrical Subsystems Design

The electrical subsystem was designed to achieve several critical functions: to supply power and control to each of the five DC motors (four pontoon motors and one ramp motor), accurate measurement of the current supplied to each motor, as well as interpretation of the encoder data from each motor and providing a controlled, closed-loop response in real time. A Raspberry Pi microcontroller was chosen as the foundation of the electronics subsystem due to its history of being capable of reliably controlling many motors simultaneously, as well as its vast network of community support. A detailed view of the electronics subsystem is shown in Figure 9.

As mentioned previously, the foundation of the electronics subsystem was a Raspberry Pi model B+, featuring a 64-bit quad-core processor with a built-in metal heat sink capable of efficient temperature regulation. This subsystem was responsible for control, performance measurement, and data storage of the CASPER prototype during its experimental data collection campaign.

The base Raspberry Pi microcontroller was fitted with multiple printed circuit boards, otherwise known as "hats", each serving a unique function. Three hats were dedicated to providing control and current measurement to the five motors responsible for operation of the CASPER prototype. These three hats were comprised
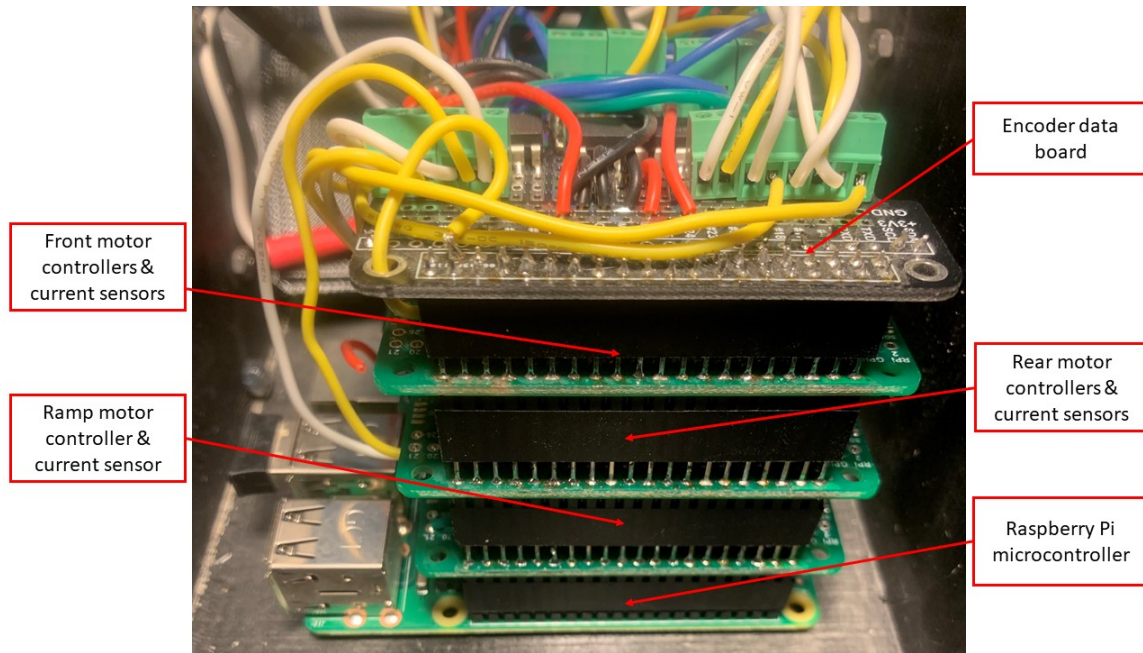
Figure 9. Electronics System with Key Features Labeled.

of Pololu MC33926 motor driver boards equipped with two Hall-effect based Pololu ACS714 current sensors. Accurate measurement of the current was determined to be necessary to guarantee that the measured power from each motor was accurate during experimentation. Starting from the base Raspberry Pi board, the first hat was responsible for controlling and measuring the current from the excavation ramp motor. Similarly, the second hat was responsible for control and current measurement of the front two pontoon motors. Finally, the third hat was responsible for control and current measurement of the rear two pontoon motors. The fourth hat, positioned above all previous three hats, was responsible for sensing the encoder data from all motors and issuing command signals based on the PD control system described in the following subsection.

The Raspberry Pi microcontroller operates on a Linux operating system. This microcontroller was controlled via a tethered HDMI connection to a monitor, as well

22

as a Bluetooth USB keyboard and mouse. After each data run, a comma separated variable file comprising the voltage, current, and RPM data for each motor was saved to the local operating system. These raw data files were extracted using a USB flash drive and were transferred to another computer for analysis. The software that runs on this electrical hardware to control CASPER and record data are described in the following section.

2.2.4   Control Methods

CASPER's control system had two primary functions: to control the angular velocity of the four screw pontoons and operate the excavation ramp. Both the ramp and pontoons were controlled by separate subroutines in a single Python script operating on the Raspberry Pi's Linux operating system. The screw pontoon control scheme will be discussed first, followed by the ramp control scheme.

Broadly speaking, the angular velocities of CASPER's screw pontoons are controlled using a proportional-derivative (PD) controller algorithm, with feedback coming from magnetic disc encoders that are integrated with each of the DC motors. A simplified block diagram of the pontoon control system for a single pontoon is featured in Figure 10.

Prior to operation of the craft, the target angular velocity was set in the preamble of the Python script. Once the motors turn on, the Raspberry Pi reads the actual angular velocity from the encoder signal for each motor. The encoders utilize magnetic discs and Hall effect sensors to detect the rotation of the motor shaft with a resolution of 20 counts per revolution, or 18°. This actual angular velocity is subtracted from the target value in order to generate the error signal. This error signal is the input of the
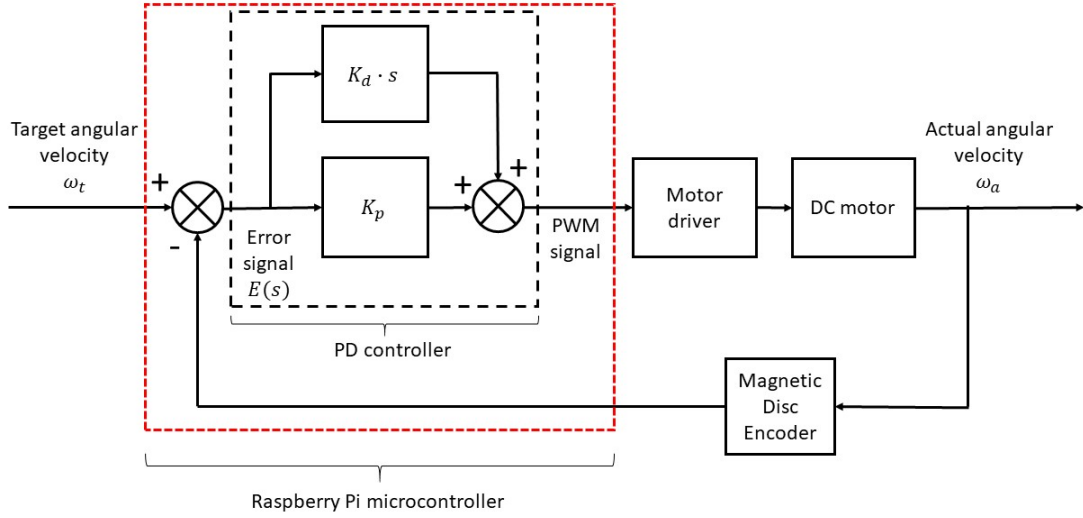
Figure 10. Simplified CASPER Pontoon Control Block Diagram.

proportional-derivative control algorithm subroutine. The mathematical description of the controller output signal [36] in the frequency domain $C(s)$ is described in Equation 2.1 below, where K_p is the proportional gain, K_d is the derivative gain, and $E(s)$ is the error signal.

$$C(s) = K_p \cdot E(s) + s \cdot K_d \cdot E(s) \tag{2.1}$$

The gains used in CASPER's pontoon control algorithm are presented in Table 2 below. Note that there are are different values of the derivative gain K_d for the front and rear motors, but the proportional gain values K_p are identical for both motors.

Table 2. Gain Values for CASPER Pontoon PD Controller

Gain	Front Motor Value	Rear Motor Value
K_p	1.0	1.0
K_d	1.2	1.5

24

These gains were tuned by examining the RPM versus time curves for each of the four motors. The primary requirements that guided the of tuning the gains were to have the motors reach steady state simultaneously, and for the settling time to be less than one second for all configurations of the test craft. It was critical to have a settling time of less than one second to guarantee that the craft was at steady state prior to the excavation cycle start, which begins two seconds after motor startup. These requirements were met through a trial-and-error process of varying the gain values while observing the angular velocity versus time plot until all requirements were met. The PD controller was implemented by structuring a loop in a Python script such that the PD term was calculated using Equation 2.1 and then used to modify the voltage output every 50 milliseconds. Using external Python packages, these voltage output values were converted into pulse-width modulation (PWM) signals and sent from the Raspberry Pi board to the motor drivers. Based on the PWM signal input, the motor driver supplies the specified voltage to the DC motor, resulting in an angular velocity that is closer to the target value.

The other major function of the control system was to control the excavation ramp. This was done without the use of any closed-loop control methods. Instead, a constant voltage with alternating polarity was supplied to the ramp motor in a hard-coded sequence to excavate material during transit. Prior to the run, the angle of the ramp relative to the floor of the craft was set to the desired value using manual inputs and a digital angle gauge. Two seconds after the start of the run, the ramp would start the excavation cycle by holding position for either two, four, or six seconds during which the ramp would make contact with the surface, and material would pile up on the forward end of the ramp. This hold duration will be henceforth referred to as the load time, and is one of several independent variables that were varied to

characterize the performance of CASPER. At the end of the load time, the ramp control script would then apply a positive voltage of 5 V to the ramp motor for 1.45 seconds. This would rotate the ramp upwards, causing the collected material to fall out the back of the ramp into the collection bin. Once in the unload position, a delay of 0.5 seconds was executed to guarantee all material was able to fall into the collection bin. Following the unload stage, a negative voltage of 5 V was applied for an identical 1.45 seconds, causing the ramp to rotate downwards and return to its starting position. Once back in the starting position, the ramp excavation cycle would begin again. For the purposes of experimental consistency, only two excavation cycles per run were performed. This limit of two cycles was determined because at maximum speed and load time, CASPER was only able to complete two cycles in the time it took to traverse the full length of the experimental test bed. The design and dimensions of the test bed will be described in the following section.

2.3   Experimental Setup

2.3.1   Experiment Test Bed

All CASPER mobility and excavation experiments were performed in the test bed that is detailed in this section. The test bed was constructed out of 0.375 inch thick acrylic panels and is held together by commercial off-the-shelf aluminum brackets and fasteners. The test bed and auxiliary equipment are shown in Figure 11. Additionally, the dimensions of the test bed including the depth of the Quikrete silica sand are detailed in Table 3.
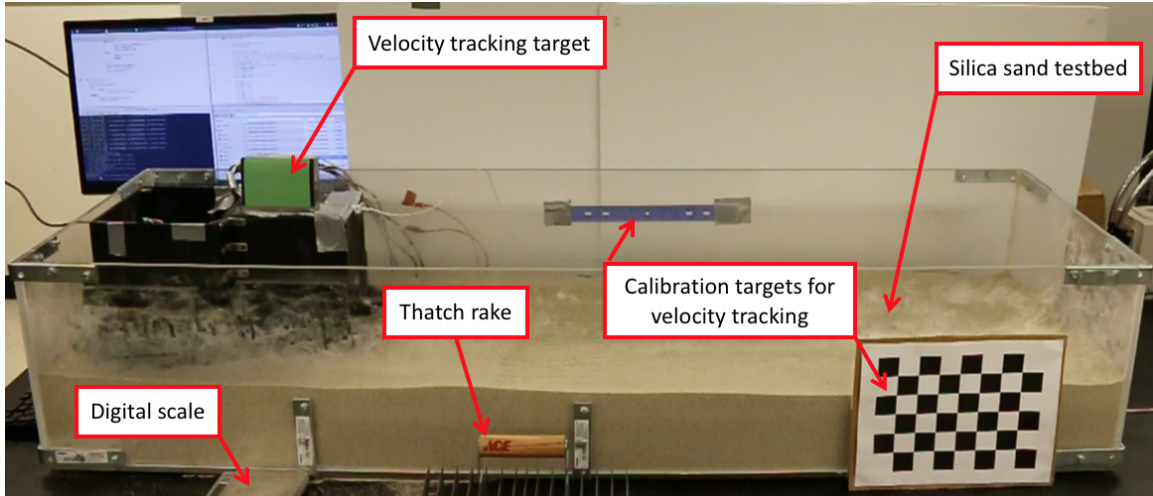
Figure 11. Experimental Test Bed with Auxiliary Equipment Labeled.

Table 3. Dimensions of Experimental Test Bed

Length	Width	Height	Sand depth
150 cm	45 cm	45 cm	20 cm

The test bed was filled with several hundred pounds of commercially available Quikrete 1962 Eglin silica sand such that the depth of the sand was 20 cm. This was done to guarantee that no wall effects from the screws being too near to the floor of the test would impact the screw pontoon performance. The relevant geotechnical properties of the Quikrete sand are reported in Table 4.

Table 4. Geotechnical Properties of Quikrete Silica Sand

Parameter	Value	Source
Mean particle diameter	0.8 - 1.8 mm	[37]
Bulk density	1.51 - 1.75 g/cm^3	[38]
Specific gravity	2.60 - 3.15	[39]
Average friction angle	17.7 $\pm$ 6.9°	[37]

One other tool shown in Figure 11 is the thatch rake. This device was used to reset the soil between each run. The exact process for this will be described in the experimental procedure section in the following chapter. This test setup was used to

27

gather the mobility and excavation performance data during a series of approximately 500 experiments. The data recording and analysis procedures are detailed in the following section.

2.3.2 Analysis Methods

In order to characterize the excavation and mobility performance of CASPER, several key parameters such as power, velocity, and excavation rate were directly measured. From these measured values, other indirect performance quantities such as cost of transport (COT) and excavation transport rate (ETR) were calculated. The process and formulae used to calculate the indirect performance measures will be discussed in the next chapter, and this section will focus on how the directly measured parameters were obtained.

The first performance measured to be discussed is the craft power consumption. Equation 2.2 was used to calculate the power consumption of the craft, where P is the power in Watts (W), I is the current in Amps (A), and V is the voltage in Volts (V).

$$P = I \cdot V \tag{2.2}$$

From this equation, it is clear that the current and voltage supplied to each motor need to be recorded to obtain the power measurement. As mentioned previously, CASPER's electronics system was fitted with Hall-effect based Pololu ACS714 current sensors. These sensors were recommended by the manufacturer specifically for use with the motor driver model because they provide a significantly more accurate current reading than the standard motor driver hardware. Using these current sensors, CASPER automatically recorded and stored the current vs. time data for each motor

from each run in a comma-separated variable file. Similarly, the voltage output for each motor was stored in the same file. From these data, the power as a function of time was calculated for each motor individually. All five motors power consumption was added together, and then the temporal average (Equation 2.3) of the steady state portion of the data was taken to obtain the total power for each run. Note that in Equation 2.3 $\overline{V_T}$ is the temporal average of the velocity, T is the time duration, and t is the integration variable. This integral was evaluated numerically via the trapezoidal method in MATLAB using a built-in function.

$$\overline{V_T} = \frac{1}{T} \int_0^T V(t)\, dt \tag{2.3}$$

For each set of unique experimental parameters, a multiplicity of five runs was completed. The final reported power data points shown in the next chapter are the ensemble average (Equation 2.4) of the power consumption for all five runs. Note that in Equation 2.4 $\overline{V}$ is the ensemble average of the time averaged velocity set, $\overline{V_{T_i}}$ are the temporal averages of the velocity from each individual run, and N is 5, the total number of trials in each set.

$$\overline{V} = \frac{1}{N} \sum_{i=1}^N \overline{V_{T_i}} \tag{2.4}$$

The velocity was measured by analyzing the video recordings of each run using a MATLAB color-tracking algorithm. Figure 11 exhibits several key features that were used to facilitate the color-tracking. A bright green rectangle was affixed to the top of the craft to serve as a velocity tracking target. A color filter was used to eliminate all features in the video other than this velocity tracking target. The filtered videos were then analyzed using the color-tracking algorithm to count the number of pixels per unit time that the target was moving. Note the ruler and checkerboard pattern

calibration targets. These targets were used to define the pixels-per-inch value that was used to translate the pixels per unit time value into velocity. Similar to the power measurements, the temporal average over the steady state period was taken using Equation 2.3 to determine the average velocity for each run, and the ensemble average of all five runs was taken using Equation 2.4 to obtain the reported data point for each set of parameters.

Finally, the excavation rate data was determined using a digital scale to weigh the collection bin after each run. The mass of the excavated material was recorded and later divided by the time duration of each run. The run duration was standard between all runs with equivalent load times because the control code was only set to operate for two cycles of the ramp mechanism. In a similar fashion to the power and velocity, the ensemble average of the five runs for a given set of parameters was calculated using Equation 2.4. The results from these analytical processes are reported and expanded upon in the following chapter.

One final key step in the analysis was determining the standard error of the experiments to indicate the variance in the performance measurements. The standard error was calculated using Equation 2.5 where σ is the sample standard deviation and N is 5, the number of trials.

$$SE = \frac{\sigma}{N} \tag{2.5}$$

The sample standard deviation was calculated using Equation 2.6 where x_i is the measured value for each of the 5 trials, $\overline{x}$ is the sample mean, and N is again 5, the number of trials.

$$\sigma = \sqrt{\frac{\sum_{i=1}^{N}(x_i - \overline{x})^2}{N - 1}} \tag{2.6}$$

The calculation of standard error was carried out in MATLAB. First, the target quantity was calculated for all individual trials. Then, for each block of five trials, the standard deviation and standard error were calculated. These values are presented as error bars featured in all plots presented in the results section.

Chapter 3

PERFORMANCE OF CASPER ISRU EXCAVATION SYSTEM

3.1   Overview

Once the craft was developed and experimental test bed and procedures were prepared, the characterization of CASPER's mobility and excavation performance was achieved through a set of approximately 500 experimental runs. During these runs, the craft would travel in a straight line through freshly tilled Quikrete silica sand while the ramp excavation system completed two cycles. The following section will describe the various configurations of CASPER that were tested, as well as detailing the independent variables that were varied to characterize the craft performance. The final section will present and discuss the results of these experiments.

3.2   CASPER Performance Experiments

3.2.1   Experimental Configurations and Independent Variables

The mobility and excavation performance experiments tested the performance of four distinct configurations of CASPER over a wide range of three independent variables. The physical characteristics of each configuration and the sets of each independent variable that were tested are listed in Table 5. A labeled front view of each configuration illustrating the various front screw rotation directions and front

pontoon widths, as well as images of the wakes left behind by each configuration are shown in Figure 12.

Table 5. Experimental Configuration Parameters

Configuration	C1	C2	C3	C4
Front separation	145 mm	145 mm	105 mm	105 mm
Churn direction	Outward	Inward	Outward	Inward
ω (RPM)	20, 30, 40	20, 30, 40	20, 30, 40	20, 30, 40
Load time (s)	0, 2, 4, 6	0, 2, 4, 6	0, 2, 4, 6	0, 2, 4, 6
Ramp Angle (°)	0, 35, 40, 45	0, 35, 40, 45	0, 35, 40, 45	0, 35, 40, 45
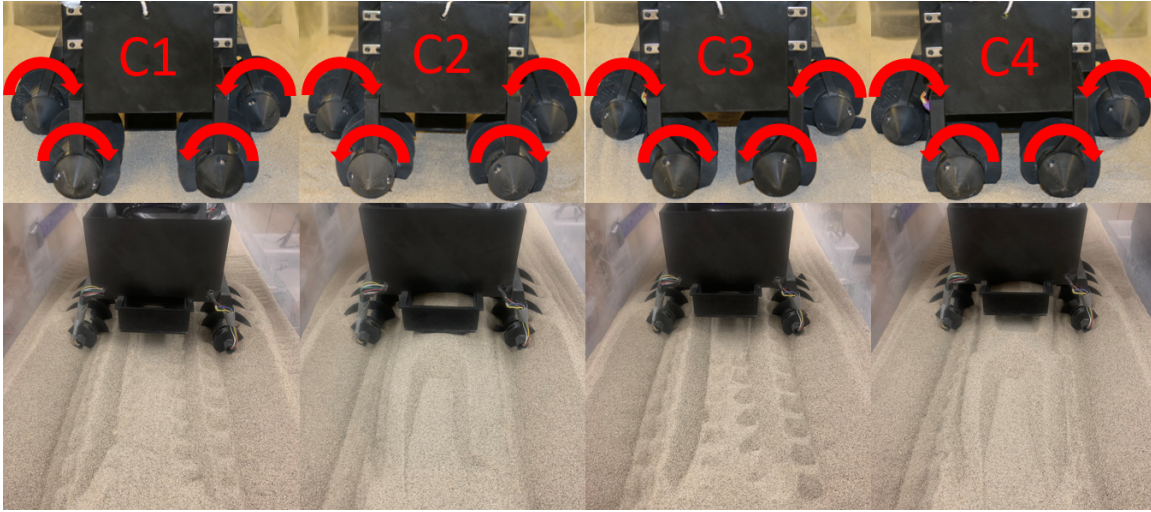
Figure 12. Front View of Each Configuration with Indicated Screw Rotation Direction and Their Corresponding Wakes.

Each configuration had a unique combination of the direction in which the material was churned by the front pontoons (inward or outward), and the front pontoon width (narrow or wide). The pontoon mounts for configurations C1 and C2 (pictured in Figure 12) create a 145 mm separation between the centers of the front pontoons. Conversely, configurations C3 and C4 have narrower pontoon mounts that create 105 mm of separation. Not only do the configurations vary the length between the front pontoons, but the direction of material churning is varied amongst them as well. The

front pontoon handedness and rotation direction are opposite of the rear screws for the even configurations C2 and C4. This causes the material to be churned inward by the front pontoons. This "inward-churning" creates a wake of loosely compacted material that is elevated with respect to the undisturbed sand. This elevated wake has multiple benefits for excavation. First, the increased height translates to less angular displacement (and thus less work) required to collect and deposit material. Second, the material being collected is loosely compacted with respect to the undisturbed sand due to the front screws churning it up prior to collection. This means less force is required by the excavation ramp to successfully collect material. Conversely, the screw handedness and rotation direction of the odd configurations C1 and C3 are identical to the rear pontoons. In all cases, the rear screw handedness and rotation direction cause the material to be churned outward and away from the central ramp, and the odd configuration front pontoons exhibit the same behavior. For each configuration, the power, velocity, and excavation rate of the craft were directly measured over a range of each of the following independent variables:

- **Angular velocity ω:** The rotation rate of each screw pontoon.
- **Load time:** The length of time where the ramp is in the downward position, in contact with the granular media, traversing forward, and excavating material.
- **Ramp angle:** The angle that the ramp makes with respect to the floor of the craft body.

It should be noted that the 0 second load time and 0° ramp angle act as the control group for the mobility power and velocity measurements. During these specific runs, the ramp was effectively disabled in the upright stowed position. Therefore, the power and velocity were unaffected by the reaction forces due to the ramp excavation.

34

The purpose of these experiments is to determine what effect, if any, the front pontoon width and material churn direction have upon the power consumption, velocity, and excavation rate of the craft across a wide variety of screw angular velocities, load times, and ramp angles. The experimental procedure is described in the next sectioned, followed by the results in the following section.

3.2.2 Experimental Procedure

Before each experimental run was initiated, the granular media was manually reset using a consistent procedure using a modified thatch rake (pictured in Figure 11. Before the reset process began, the craft would be removed from the soil. Next, the tines of the thatch rake was drawn along the longitudinal axis of the test bed until the material was no longer compacted. Following this, the thatch rack tines were drawn in the transverse direction. Finally, visual inspection of the sand level was performed and minor movements of sand took place until the surface of the sand was flat and level, such that the volume fraction was constant between runs. This process was performed to minimize the variance in measured quantities due to a buildup of plastic deformation in the sand. Inconsistent soil conditions cause variability in the interactions of the mobility system and the granular media [40], which increases the variance in the measured performance parameters.

After the Quikrete silica sand was reset between trials, the craft was placed back at the left end of the test bed. From here, the ramp angle was measured using a digital angle gauge, and the ramp would be rotated using command line inputs until the angle was within 0.1 ° of the target ramp angle. After the inter-trial procedure was complete, the control program was launched at the command line to start the

run and the Nikon camera was set to record. Once enabled, the craft would move forward for two seconds to allow the mobility system to achieve steady state. Following the two-second delay, the ramp excavation subroutine executed two cycles of ramp actuation, after which the run was concluded. Two excavation cycles were chosen because this is the maximum amount of cycles possible in this length of a test track at the highest screw angular velocity of 40 RPM with the longest load time of 6 seconds. Finally, the camera recording was stopped and the the collection bin was removed. Using a digital scale, the excavated mass was weighed and the resulting value was recorded. This process was repeated for a multiplicity of five trials per experimental configuration to improve the accuracy of the reported performance values.

3.3   Results

As mentioned in the previous section, the purpose of these experiments was to quantify the effect the material churn direction and front pontoon width have upon the power consumption, velocity, and excavation mass performance of the craft across a wide variety of screw angular velocities, load times, and ramp angles. In the following subsections, the experimental data for the excavation rate, power, velocity, cost of transport, and excavation transport rate are presented and analyzed. Based upon these results, optimal configuration and parameter sets are identified. In the next chapter, the mobility and excavation performance of CASPER is compared to both continuous and discrete excavation systems found in the literature. Note that in all figures, the error bars represent the standard error, which was calculated using the methods described in Section 2.3.2.

3.3.1 Excavation Rate

Figure 13. Comparison of Average Excavation Rate (kg/hr) vs. Load Time (s) Between All Configurations for Ramp Angles of 35°, 40°, and 45°, and Screw Rotational Velocities of 20, 30, and 40 RPM.

Figure 13 illustrates that CASPER's excavation rate behavior is relatively well behaved. In other words, the excavation rate follows quasi-linear increasing trends with respect to both the load time and angular velocity. The ramp system was unable to collect any granular media at ramp angles of 35° and 40° for both the wide and narrow outward-churning configurations C1 and C3. Even when the ramp angle was increased to 45°, the outward-churning configurations C1 and C3 were only able to excavate at the higher angular velocities. For the wider outward churning configuration C1, the material was able to be excavated at 30 and 40 RPM. However, for the narrower outward churning configuration C3, material was only able to be excavated at 40 RPM. As a whole, the fact that the outward churning capability cannot excavate material at lower ramp angles illustrates the superiority of the inward-churning configurations

with respect to the excavation capability. In addition, the ramp motor requires less angular displacement and thus, less work to deposit the material in the collection bin. This benefit arises from the fact that the inward-churning configurations have an elevated wake of material trailing the front screws.

As one might expect, the excavation rate follows an increasing trend as the screw angular velocity increases. This trend can be explained by considering the impact of the increasing angular velocity. As the angular velocity increases, the linear velocity of the craft increases. The increasing linear velocity leads to a greater mass flux of granular media flowing onto the ramp edge, which allows the material to build up to a greater height on the blade itself prior to the ramp rotation. The mechanism that causes the excavation rate to increase as the load time increases is similar to what causes the excavation rate to increase with the angular velocity. By increasing the load time, the granular media is given more time to build up in front of the leading edge of the ramp before the ramp motor is engaged to rotate the ramp and deposit the excavated material in the collection bin. The increase from two to four seconds in load time yields a much higher marginal increase in excavation rate in comparison to the marginal increase from four to six seconds. In other words, there appears to be a bit of a diminishing returns phenomenon with respect to load time.

Ultimately, the peak excavation rate of 30 kg/hr was achieved with both the narrow and wide inward-churning configurations C2 and C4. These configurations were able to attain this excavation rate only at the highest angular velocity of 40 RPM and with higher load times of 4 and 6 seconds. This implies that peak excavation rates are achieved when the combination of angular velocity and load time causes the maximum amount of material to build up on the ramp prior to rotation.
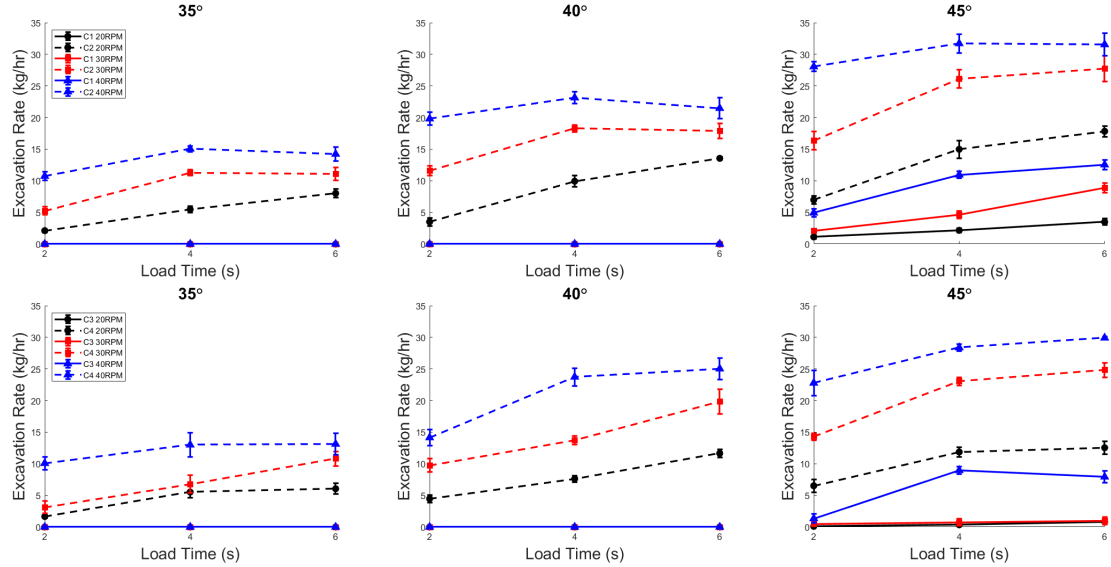
3.3.2 Power

Figure 14. Comparison of Average Total Power (w) vs. Load Time (s) Between All Configurations for Ramp Angles of 35°, 40°, and 45°, and Screw Rotational Velocities of 20, 30, and 40 RPM.

Next, the impacts of the independent variables upon CASPER's power consumption are discussed. As shown in Figure 14, the total craft power consumption increases significantly as the screw angular velocities are increased. Increasing the angular velocity increases the mechanical power output of the screw pontoon motors, so it makes sense that the electrical power would increase as well. The total power consumption is approximately 15-18 W for the 20 RPM angular velocity cases, while the power draw is roughly 25-28 W for the 40 RPM cases. This trend indicates that the increase in power is quasi-linear with respect to RPM. Less intuitively, the power was found to be approximately constant with minor fluctuations with respect to the load time for a given configuration and angular velocity. It is apparent that the ramp-terrain interaction would create a large drag force that would increase as the

speed of the vehicle increases. Upon initial consideration, one might hypothesize that increasing the angular (and by extension, linear) velocity would result in a higher drag force, and therefore increase the power required to maintain the velocity. However, this was found to not be the case. Recall that the ramp did not make contact with the soil for the outward churning configurations C1 and C3. For these configurations, Figure 14 indicates that the power draw is nearly identical to the no ramp control case (0 seconds load time). For the inward-churning configurations C2 and C4, where the ramp did make contact with the soil, it was found that the power draw increases slightly above the no ramp level.

It is important to point out that the majority of the power draw was consumed by the the four motors powering the screws. The excavation ramp DC motor had a negligibly low power draw of between 0.1-0.2 W, which is approximately two orders of magnitude less than the total power consumption. The fact that the mobility system consumes the majority of the power, coupled with the fact that the power consumption does not increase considerably with higher load times, implies that the most efficient configuration for this system is the one that maximizes the excavation rate. Here, efficiency is defined as the power consumed per unit excavation rate. In order to further investigate this hypothesis, the excavation transport rate (ETR) was analyzed, and the results are discussed in a later section.

As we saw in the previous section, the maximum excavation rate corresponded to configurations C2 and C4, operating at 40 RPM with a 4-6 second load time. These most productive configurations and parameter combinations consumed between 25 and 30 W. This is a relatively low amount of power, which bodes well for the potential of using the CASPER architecture for planetary surface ISRU applications because space systems typically seek to minimize the mass and power requirements.

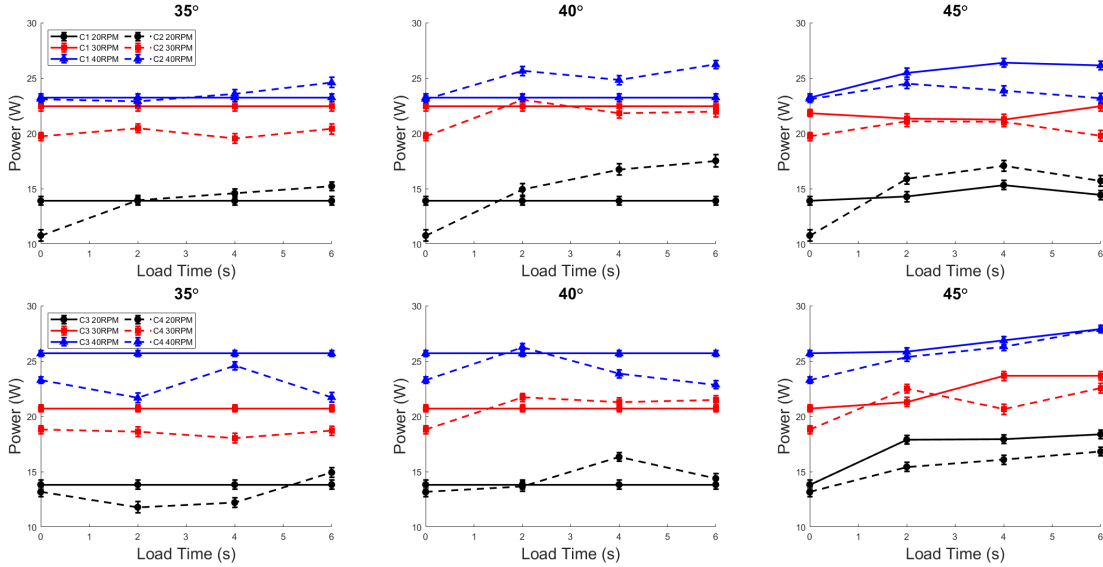### 3.3.3 Front Power Ratio

Figure 15. Comparison of the Average Ratio of Front Power vs. Load Time (s) Between All Configurations for Ramp Angles of 35°, 40°, and 45°, and Screw Rotational Velocities of 20, 30, and 40 RPM.

The front power ratio is defined as the ratio between the average power consumption of the front two screws and the mobility power (power draw of all four screws). For all experimental cases, the front power ratio exhibited moderate fluctuations between 0.25 and 0.4. Figure 15 shows that the front power ratio is essentially constant with respect to load time and exhibits a slight increase as RPM increases. Interestingly, the ramp angle, churn direction, and front pontoon width appear to have no impact upon the front power ratio. One potential explanation for the fact that the front pontoons consume less power than the rear ones is that the front pontoons experienced undisturbed granular media. Conversely, the rear pontoons required more power to achieve the target RPM because they encountered the trailing wake of the front pontoon which was less compacted.

3.3.4 Velocity

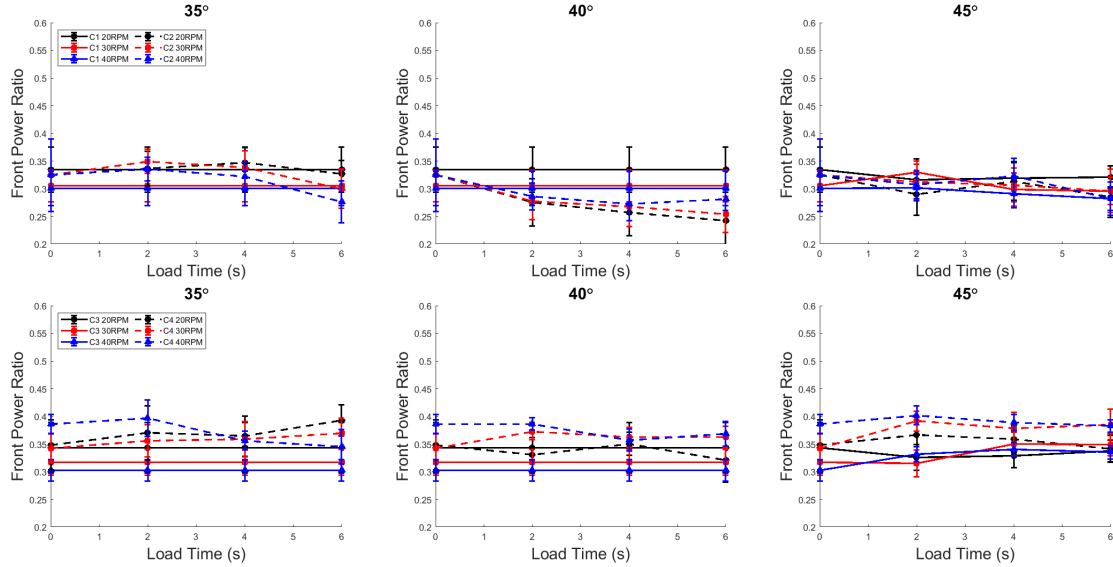
Figure 16. Comparison of Average Craft Velocity vs. Load Time (s) Between All Configurations for Ramp Angles of 35°, 40°, and 45°, and Screw Rotational Velocities of 20, 30, and 40 RPM.

Recall from the excavation rate subsection that the linear velocity of the craft was intimately linked to the magnitude of the excavation rate. Thus, the linear velocity of the craft is a very relevant quantity when quantifying the mobility and overall performance of an excavation vehicle. CASPER's velocity distribution across all independent variables is presented in Figure 16. As mentioned in previous sections, increasing the angular velocity of the screws leads to an increase in the linear velocity of the craft. At 20 RPM, the linear velocity of the craft is approximately 5 - 6 cm/s, and the 30 and 40 RPM cases are approximately 8-12 and 15-20 cm /s, respectively. This trend implies that an increase in screw angular velocity produces an approximately linear increase in craft linear velocity. This pattern has been demonstrated previously in the literature [31, 34, 33, 32] and serves as a sanity check for the velocity results.

Upon observation of Figure 16, it is readily apparent that the velocity is fairly constant with respect to the load time, as well as the ramp angle.

The velocity distribution indicates that there is no significant difference between the wide configurations C1 and C2. Conversely, the narrow configurations C3 and C4 exhibit substantial differences. Specifically, the outward-churning configuration C4 achieves dramatically lower velocities than the inward-churning C3. The mechanism behind this disparity is currently unknown. Potentially, this discrepancy between the inward and outward churning narrow configurations is explained by how the front pontoon width changes the position of the front pontoon wake. When the craft is in the wider configurations C1 and C2, the rear pontoons are only slightly inset with respect to the rear pontoons. As a result, the rear pontoons are constantly engaging in media that has already been churned. Conversely, the front pontoons are almost entirely out of the way of the rear pontoons for the narrow configurations C3 and C4. When the front pontoons are churning inward, the rear pontoons are engaged with essentially undisturbed granular media because the wake material is deposited in between the rear screws. This causes the rear pontoons to produce more thrust force than the outward churning case where the wake material is deposited in the path of the rear pontoons. This effect is likely also present in the wide configuration, but has less impact regardless of the churn direction due to the fact that the front and rear pontoons are nearly in line with each other. The data indicate that the maximum velocity of approximately 18.7 cm/s (11.2 m/min) is achieved in the same C4 configuration operating at 40 RPM with a 4 second load time that produces the highest excavation rate, which indicates that this configuration and parameter set offers the best performance.
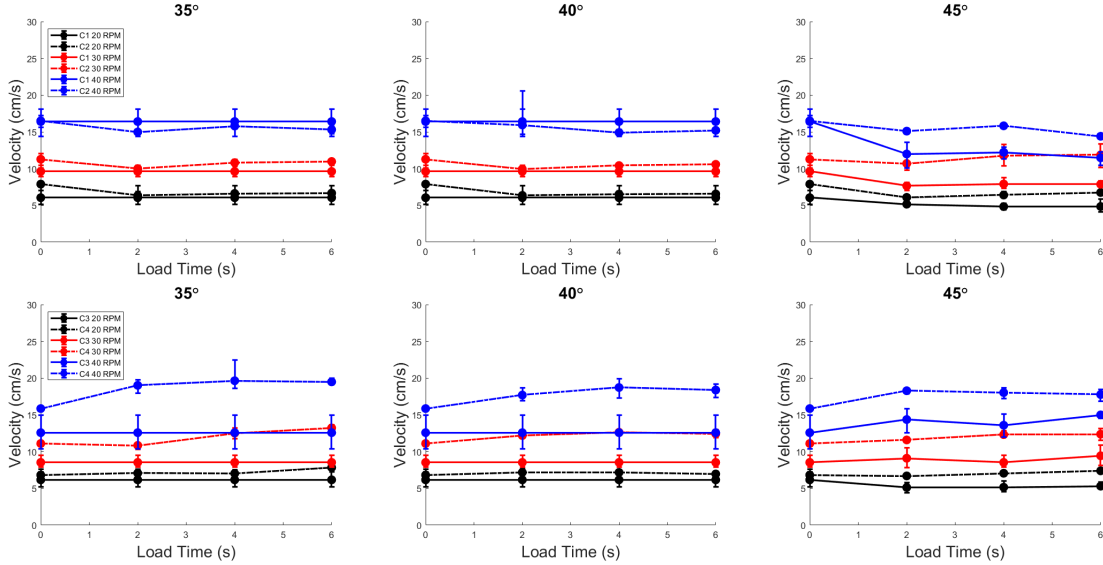
3.3.5 Cost of Transport

Figure 17. Comparison of Average Cost of Transport vs. Load Time (s) Between All Configurations for Ramp Angles of 35°, 40°, and 45°, and Screw Rotational Velocities of 20, 30, and 40 RPM.

The cost of transport (COT) is a quantity that is used to characterize how efficient a mobility system is based on the weight of the system, the magnitude of the velocity, and the power required to drive the mobility system. Traditionally, the cost of transport has not been used to analyze the effectiveness of ISRU excavation systems. However, the cost of transport has been shown in the literature [41] to be an effective means of characterizing the mobility performance of robots in granular media. Therefore, the COT of the CASPER prototype was analyzed to quantify it's mobility performance. The cost of transport is defined in Equation 3.1, where P is the craft power consumption, m_c is the total mass of the craft, g is the acceleration due to gravity, and V is the linear craft velocity.

$$COT = \frac{P}{m_c \cdot g \cdot V} \tag{3.1}$$

Figure 17 shows the distribution of the cost of transport results across all independent variables. Upon examination, it is readily apparent that the cost of transport reduces as the RPM increases. However, it is also evident that the cost of transport is not significantly impacted by load time. Furthermore, the results illustrate that the cost of transport increases as the ramp angle increases. This indicates that the increased drag force from a lower ramp angle does indeed impact the mobility performance. Additionally, it was found that the inward-churning configurations had a lower cost of transport when compared to the outward-churning configuration. The reason behind this is likely due to the previously mentioned phenomenon where the rear screws of the inward-churning configurations make contact with virtually undisturbed media while the rear screws of the outward-churning configurations do not. A comparison of the top and bottom rows of Figure 17 indicates that the narrow/wide configurations have roughly the same cost of transport at all angular velocities and load times. Finally, it can be concluded that higher angular velocities of 30 and 40 RPM yield the lowest cost of transport. Altogether, the cost of transport trends imply that the higher RPM cases move the fastest for a given amount of power, and thus are more efficient for mobility in granular media. In the next section, a new quantity, the excavation transport rate, will combine the cost of transport and excavation rate. Investigation of this novel parameter gives insight on the combined mobility and excavation performance of the CASPER prototype. The minimum cost of transport of approximately 4 was achieved by the C4 configuration operating at 40 RPM with a 4-6 second load time, which confirms that this is the most efficient combination of operational parameters and configuration.

3.3.6 Excavation Transport Rate

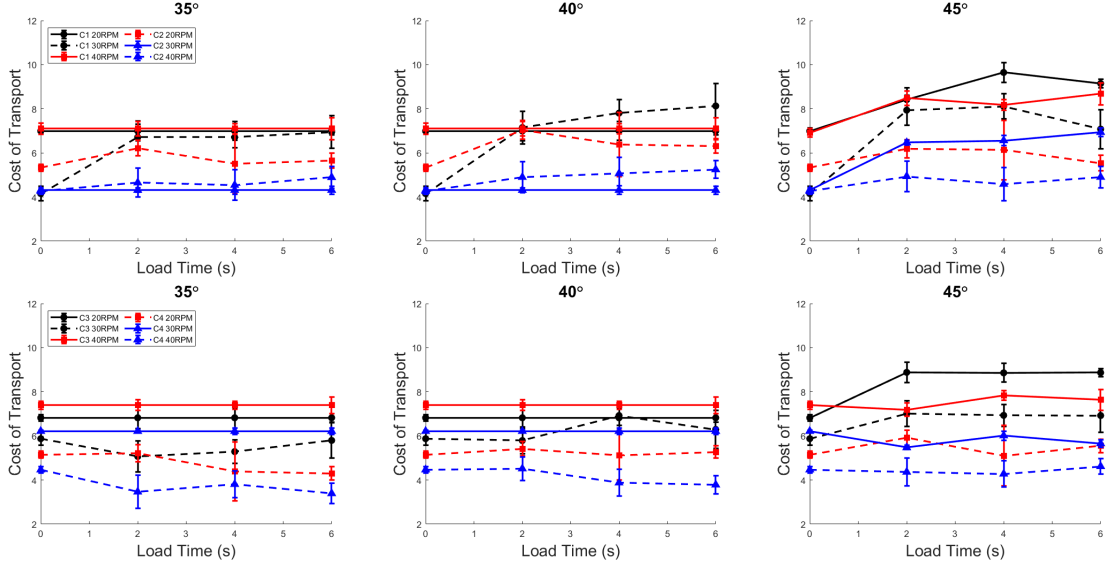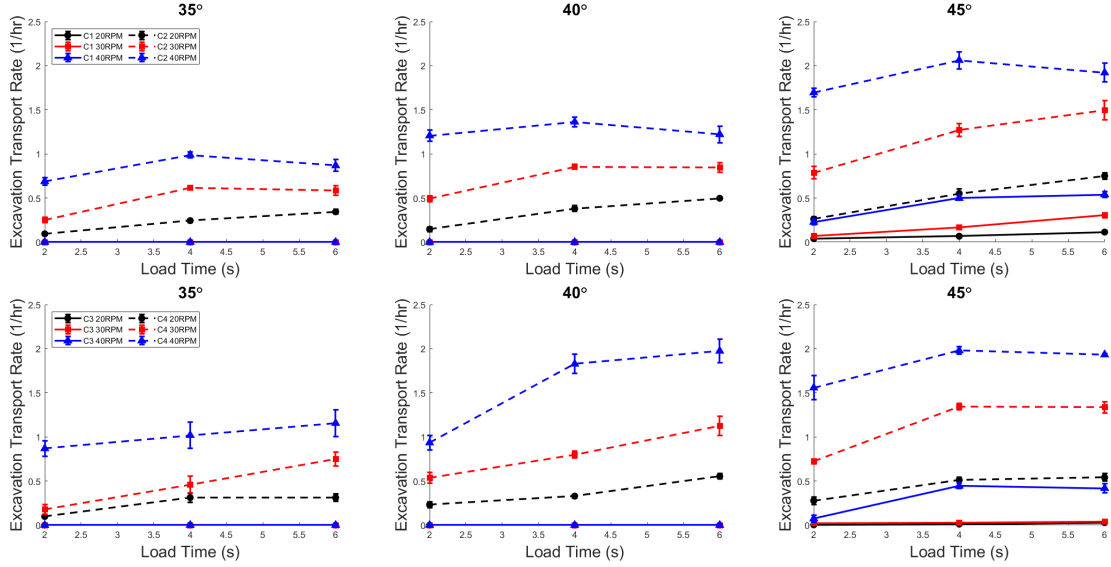Figure 18. Comparison of Average Excavation Transport Rate of Transport vs. Load Time (s) Between All Configurations for Ramp Angles of 35°, 40°, and 45°, and Screw Rotational Velocities of 20, 30, and 40 RPM.

The excavation transport rate (ETR) is a novel parameter introduced in this work that can represent the overall transportation and excavation efficiency of a hybrid mobility-excavation system. ETR is defined in Equation 3.2, where R_E is the excavation rate, m_c is the craft mass, and COT is the cost of transport.

$$ETR = \frac{R_E}{m_c \cdot COT} \tag{3.2}$$

In essence, the ETR normalizes the excavation rate by the cost of transport in order to shed light on the combined mobility and excavation performance. It is advantageous to consider the mobility and excavation performance together when evaluating ISRU excavators because they must be capable of both excavation and efficient mobility on planetary surfaces. Additionally, the ETR normalizes the excavation rate by

46

the weight of the system so that comparisons between large and small excavation systems are more informative. It should be noted that a higher value of ETR provides higher performance because more mass is being collected at a lower system mass cost of transport. The distribution of ETR data across all independent variables is shown in Figure 18. These plots illustrate ETR trends that are consistent across all configurations, angular velocities, and load times. As the load time increases, the ETR increases in a quasi-linear fashion. A similar trend exists between ETR and angular velocity. Increasing the angular velocity from 20 to 30 RPM yields a similar increase in ETR as increasing it from 30 to 40 RPM in almost all cases. There does not appear to be a significant difference between the wide and narrow configurations C2 and C4, as both of these follow very similar trends and end up approaching the same maximum ETR values at each given ramp angle.

Note that only the 45° cases have nonzero values for C1 and C3. This is due to the fact that these cases were the only ones that had nonzero excavation rates. Figure 18 indicate that the inward-churning configurations C2 and C4 have significantly higher ETR values when compared to the outward-churning configurations C1 and C3. This dramatic difference is illustrative of the fact that the inward-churning configurations have similar cost of transport in comparison to their outward-churning counterparts, however they are significantly better at excavation. Additionally, it is evident that the most efficient configurations are achieved by increasing the ramp angle, load time, and angular velocity. Moreover, there does not appear to be a significant difference in ETR between the four and six second load time cases for both outward churning configurations at the 40° and 45° ramp angles. These would appear to be the most efficient configuration of all settings. In a space environment, one might opt for 30 RPM which would be operating at less than peak efficiency, but with lower total power

47

required. The lower angular velocity would provide a lower total power requirement, which in turn would lower the mass of the spacecraft. For terrestrial applications, it would be likely to favor the faster angular velocity which would maximize the excavation rate. Ultimately, it appears that there is an optimum ETR value that can be achieved with many different configurations of load time, ramp angle, and angular velocity.

In general, it was found that the inward-churning configurations C2 and C4 were able to collect significantly more mass at practically the same total power while traveling at the same or greater speeds in comparison to their outward-churning counterparts C1 and C3 across all load times, ramp angles, and angular velocities.

During the experiments, it was observed that the inward-churning configurations created an elevated wake behind the front screws, directly in the path of the ramp. Conversely, the outward-churning configurations left a strip of undisturbed flat sand in front of the ramp because the front screws diverted the sand away from the ramp. A detailed image of the wake patterns for each configuration is shown in Figure 12. It is noteworthy that the length of the depression cut by the ramp is directly proportional to the load time, with larger load times leaving longer cuts in the granular media. Additionally, the ramp angle needed to be 45 degrees to just barely make contact with the soil since the outward-churning configurations did not have the elevated wake. As a result, C1 and C3 were only able to collect mass at the 45 degree ramp angle. Attempts were made to collect material at 35 and 40 degrees, but were unsuccessful. This phenomenon makes it evident that having the front screws churn material inward provided a significant benefit to act as an auxiliary mechanism for excavation.

Chapter 4

COMPARISON OF CASPER PERFORMANCE TO EXISTING ISRU EXCAVATION SYSTEMS

4.1 Comparison Target Overview

In the previous chapter, the CASPER mobility and excavation performance data were presented. In this chapter, the performance figures from the CASPER's highest performing combination of parameters and configurations are compared to several discrete and continuous excavation systems, some of which were introduced in the first chapter. The highest performance variant of CASPER that yielded the maximum ETR was the C4 configuration operating at 40 RPM with a 4 second load time, and all comparisons made henceforth will utilize the performance values corresponding to that combination of configuration and settings. The discrete excavation systems used for comparison are the back-loading backhoe system and the Cratos scraper. Additionally, the continuous excavation systems comparison targets are the bucket ladder system, mounted on the same mobility platform as the backhoe, and the bucket wheel system mounted on the Polaris mobility platform. The following sections will compare CASPER with these systems on the basis the mobility, excavation, and combined performance. The mobility performance will be assessed using velocity and cost of transport. The excavation performance comparison will be done based on the excavation rate and specific excavation rate (excavation rate/system mass) of each system. Finally, the excavation transport rate of each system will be used to compare the combined performance of all systems.

4.2 Mobility Performance Comparison

The mobility performance parameters for CASPER and the examined discrete excavation systems are presented in Table 6 below. Note that the velocity of the Cratos scraper system was estimated based on available information because it was not directly reported in the literature. It was reported that the Cratos system made 6 collections and traversals of approximately ten meters in a ten minute time frame [42]. Assuming the craft was collecting material for approximately 20% of the time, it is reasonable to assume that the traverse rate is on the order of 5 meters per minute.

Table 6. Mobility Performance Parameters for CASPER and Discrete Excavation Systems

System	Type	Mass	Power	Velocity	COT	Source
CASPER	Screws	3.35 kg	26.3 W	11.2 m/min	4.28	N/A
Cratos	Tracks	80 kg	< 100 W	5 m/min	1.53	[16, 18, 42]
Backhoe	Wheels	76 kg	< 200 W	8 m/min	2.01	[16, 43]

A visual comparison of the velocity and cost of transport between CASPER and the other discrete excavation systems is shown in Figure 19.
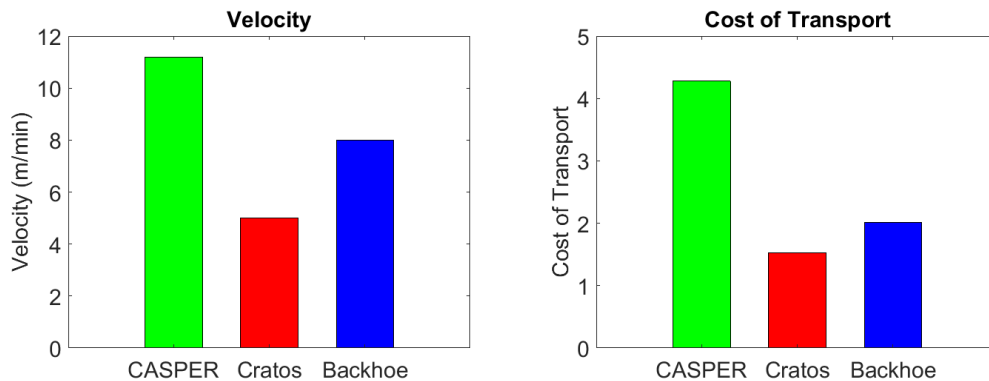

Figure 19. Comparison of CASPER Velocity and Cost of Transport to Discrete Excavation Systems

Figure 19 indicates that CASPER attains a greater velocity at a higher cost of transport in comparison to the Cratos and backhoe excavation systems. From Table 6 it is evident that both Cratos and backhoe have masses that are more than a factor of 20 greater than the mass of CASPER. Due to the lower overall system mass, CASPER is able to move significantly faster than both systems with a fraction of the power requirement. However, despite the lower overall mass and power consumption, CASPER has a higher cost of transport. This means that CASPER's screw-propelled mobility system is less efficient from a mobility standpoint than the Cratos tracks or the backhoe wheeled mobility system. Even though it is less efficient regarding mobility, CASPER's lower mass and power requirements make it more suitable for planetary surface applications, especially when one considers that the screws serve a dual-purpose by augmenting the excavation system.

Next, CASPER's mobility performance will be compared with the continuous excavation systems: the bucket ladder system and the bucket wheel system mounted on the Polaris mobility platform. The mobility performance parameters for CASPER and the examined continuous excavation systems are presented in Table 7.

Table 7. Mobility Performance Parameters for CASPER and Continuous Excavation Systems

System	Type	Mass	Power	Velocity	COT	Source
CASPER	Screws	3.35 kg	26.3 W	11.2 m/min	4.28	N/A
Bucket ladder	Wheels	76 kg	< 200 W	8 m/min	2.01	[16, 43]
Bucket wheel	Wheels	200 kg	470 W	24 m/min	0.60	[16, 23, 24]

A visual comparison of the velocity and cost of transport between CASPER and other continuous excavation systems is shown in Figure 20.

From Figure 20 it is readily apparent that CASPER has a significant disadvantage in comparison to the bucket ladder and bucket wheel systems in regard to mobility.
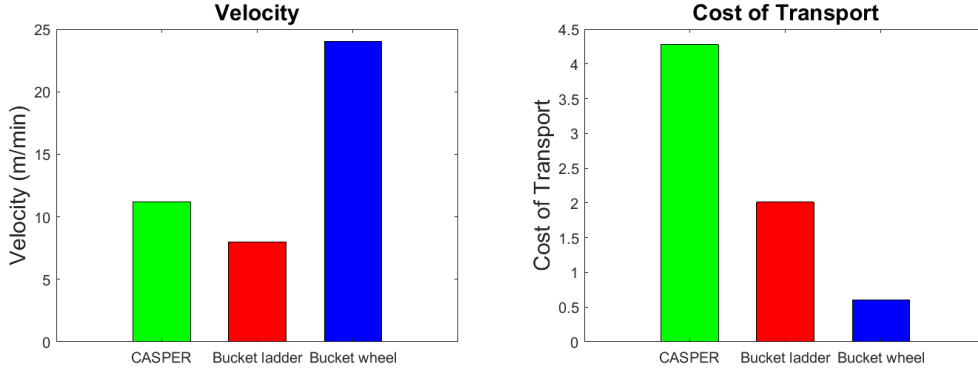
Figure 20. Comparison of CASPER Velocity and Cost of Transport to Continuous Excavation Systems

Clearly, the Polaris wheeled mobility system is superior to both CASPER and the bucket ladder/backhoe mobility system because it attains the highest velocity at the lowest cost of transport. As we saw with the backhoe, which uses the same mobility system as the bucket ladder, CASPER achieves a greater velocity, but at roughly double the cost of transport. From these data, one can easily conclude that CASPER's screw-propelled mobility system is inferior to wheeled and tracked mobility systems. This makes sense, because screws are rarely used in both planetary surface and terrestrial mobility applications. Despite their sub-par mobility performance, CASPER's screws augment the mobility system, which leads to an overall performance benefit when mobility and excavation are considered together.

4.3 Excavation Performance Comparison

Next, the excavation performance of CASPER is compared to the same discrete and continuous excavation systems outlined in the previous section. The excavation performance parameters for CASPER and the examined continuous excavation systems are presented in Table 8.

Table 8. Excavation Performance Parameters for CASPER and Discrete Excavation Systems

System	Mass	Excavation Rate	Specific Ex. Rate	Source
CASPER	3.35 kg	28.4 kg/hr	8.5 (1/hr)	N/A
Cratos	80 kg	900 kg/hr	11.3 (1/hr)	[16, 18, 42]
Backhoe	76 kg	100 kg/hr	1.3 (1/hr)	[16, 43]

A visual comparison of the excavation rate and specific excavation rate between CASPER and the other discrete excavation systems is shown in Figure 21.

Figure 21. Comparison of CASPER Excavation Performance to Discrete Excavation Systems

Upon examination of Figure 21 it is clear that CASPER has a very low nominal excavation rate in comparison to the other discrete systems examined. However, when one considers the specific excavation rate, which is the excavation rate normalized by the craft mass, CASPER is shown to have considerably good excavation performance. The backhoe is the least effective excavator overall, with low excavation and specific excavation rates. Conversely, the Cratos scraper exhibits the best excavation performance in both parameters. In conclusion, CASPER is able to deliver adequate performance in a much smaller form factor in comparison to other discrete excavators. Next, CASPER's excavation performance will be compared to the continuous excavators.

Table 9. Excavation Performance Parameters for CASPER and Continuous Excavation Systems

System	Mass	Excavation Rate	Specific Ex. Rate	Source
CASPER	3.35 kg	28.4 kg/hr	8.5 (1/hr)	N/A
Bucket ladder	76 kg	800 kg/hr	10.5 (1/hr)	[16, 43]
Bucket wheel	200 kg	1050 kg/hr	5.3 (1/hr)	[16, 23, 24]

A visual comparison of the excavation rate and specific excavation rate between CASPER and continuous excavation systems is shown in Figure 21.
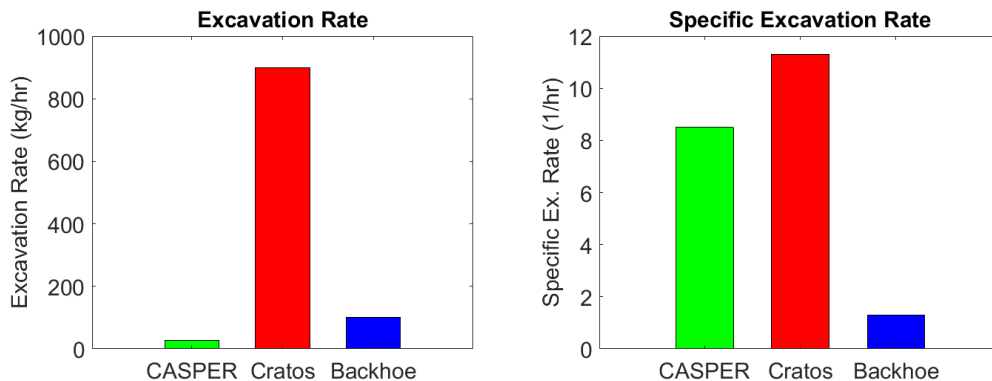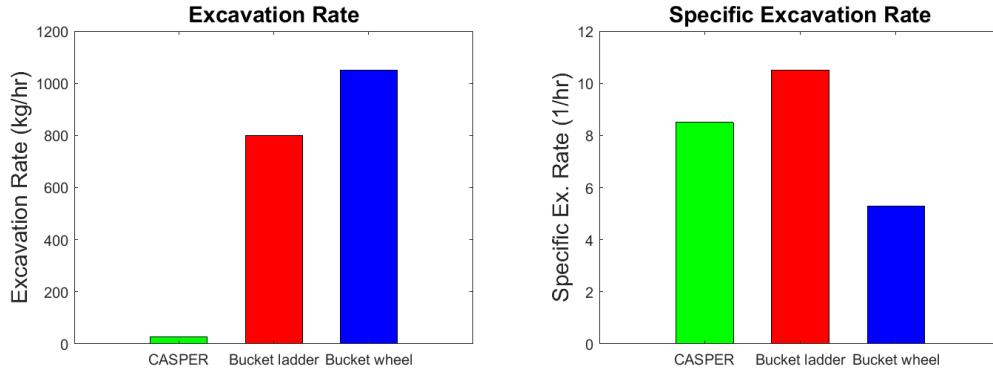

Figure 22. Comparison of CASPER Excavation Performance to Continuous Excavation Systems

Similar to the discrete excavators, Figure 22 clearly illustrates that CASPER has the lowest nominal excavation rate in comparison to the other continuous systems examined. Once again, when the specific excavation rate is investigated, CASPER is shown to have good excavation performance, especially considering how low the total mass of CASPER is. The bucket ladder is the most effective excavator in terms of specific excavation rate, and ranks second in nominal excavation rate. On the other hand, the bucket wheel delivers the highest excavation rate of any system examined, but has the worst specific excavation rate of all systems with the exception of the backhoe. The comparison to continuous excavators confirms that CASPER is able to deliver good excavation performance in a very small package, which makes it an

intriguing candidate for planetary surface applications since it would be much cheaper to launch. In the next and final section of this chapter, the combined excavation and mobility performance of CASPER is compared against the same group of excavation systems.

4.4 Combined Performance Comparison

The comparison of CASPER's combined mobility and excavation performance to other discrete and continuous excavation systems will be performed on the basis of the excavation transport rate, the novel parameter introduced in Chapter 3. The ETR data for CASPER and the discrete and continuous excavation systems are reported in Table 10.

Table 10. Combined Performance Parameters for CASPER and Continuous and Discrete Excavation Systems

System	Type	ETR	Source
CASPER	Discrete	1.98 (1/hr)	N/A
Cratos	Discrete	7.35 (1/hr)	[16, 18, 42]
Backhoe	Discrete	0.65 (1/hr)	[16, 43]
Bucket ladder	Continuous	5.23 (1/hr)	[16, 43]
Bucket wheel	Continuous	8.75 (1/hr)	[16, 23, 24]

Bar plots illustrating the comparison of ETR between CASPER and the discrete and continuous excavation systems are shown in Figure 23. Note that the comparisons for the discrete and continuous systems are presented in two separate plots.

Examination of Figure 23 and Table 10 makes it clear that as a combined mobility and excavation system, CASPER is not as effective as the majority of the systems examined. Although CASPER demonstrates ETR superiority over the widely used
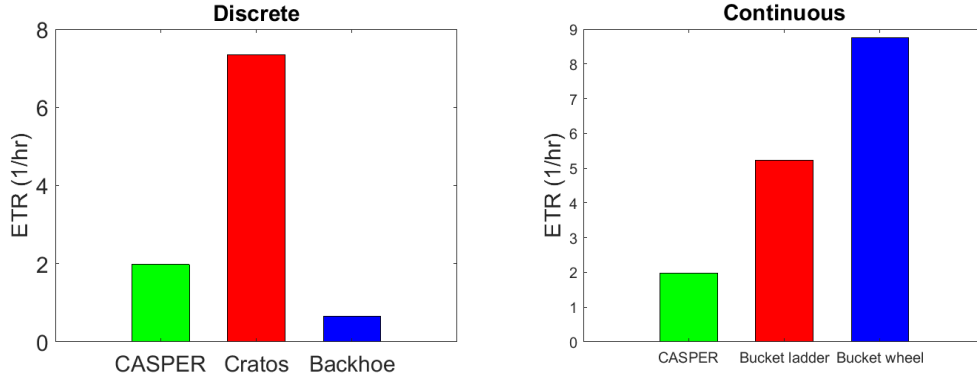
Figure 23. Comparison of CASPER Combined Performance to Continuous and Discrete Excavation Systems

backhoe system, it does not outperform any of the other systems. Despite the fact that CASPER does not outperform these other systems, it's ETR value is of the same order of magnitude of the other system's ETR values. This means that it does provide serviceable combined mobility and excavation performance, which is a significant achievement for a first generation prototype that is significantly less massive than all of the excavation systems it was compared to. This comparison provides additional evidence to confirm the hypothesis that continuous excavation systems are generally more advantageous options for planetary surface ISRU excavation applications [23]. The reason for this is because the both continuous excavators outperformed CASPER, and the bucket wheel continuous excavator had the highest combined performance of all examined excavators. Ultimately, the screw propulsion system seem to be an effective augmentation to a discrete excavation system because they provided higher performance than the backhoe system using a ramp system, which is quite similar in concept to the backhoe.

Chapter 5

CONCLUSIONS AND FUTURE RESEARCH

5.1   Conclusions

The overarching goal of this research was to develop and quantify the mobility and excavation of a novel discrete scooper excavation system. To achieve this goal, the Counter-Rotating Archimedes Screw-Propelled Excavation Rover (CASPER) was developed. The CASPER prototype was built using 3D printed and commercial-off-the-shelf parts, and the total mass of the prototype was 3.35 kg. CASPER's mobility system is comprised of four counter-rotating Archimedes screw pontoons. These screw pontoons serve dual-purpose both as the mobility system, and also as an augmentation to the excavation system. The front screw pontoons are positioned narrower than the rear pontoons, and a ramp excavation system is affixed to the craft body between the rear screw pontoons. As the craft moves forward, the front screws churn up granular media and leave behind an elevated wake of loosely compacted material which is then scooped up by the actuated ramp prior to being deposited into a collection bin which is placed in the rear of the craft.

The mobility and excavation performance of CASPER was determined by performing a set of over 500 experiments where the craft traveled in a line through Quikrete silica sand while simultaneously excavating material. Four major configurations of CASPER were investigated, consisting of narrow and wide variants of inward and outward churning front screws. These configurations were tested over a wide range of the following independent variables: ramp load time, screw angular velocity, and ramp

angle. The primary performance parameters that were measured measured included excavation rate, power consumption, and velocity. From these primary performance results, secondary performance parameters were calculated, including the cost of transport, and a new parameter, the excavation transport rate. The purpose of the excavation transport rate is to combine the mobility and excavation performance parameters into one quantity, which simplifies the comparison of ISRU excavation systems.

It was found that configuration of CASPER and settings that yielded the maximum ETR was configuration C4 operating at 40 RPM with a 4 second load time and a ramp angle of 45 °. This optimal configuration of CASPER yielded an excavation rate of around 28.4 kg/hr, a peak velocity of 11.2 m/min, while consuming 26.3 W of power. From these primary values, the cost of transport was found to be 4.28, and the excavation transport rate was found to be 1.98. The operational power of CASPER ranged from approximately 10-15 W for 20 RPM cases up to 20-25 W for the 40 RPM cases and exhibited very little variation with respect to load time. The velocity performance exhibited similar trends to the power consumption, with velocities ranging from 5-18 cm/s for 20-40 RPM with very little variation with load time. The cost of transport results indicated that higher angular velocities are more efficient for mobility, insofar as they move quicker for a given amount of power. During the experiments, it was discovered that the outward churning configurations were ineffective due to the fact that they did not create the elevated wake of pre-churned material in front of the ramp that the inward churning configurations did. According to the ETR results, the narrow and wide configurations were very similar. However, the narrow configuration have a slight ETR advantage at lower ramp angles. This is likely due to the height of the elevated wake behind the front pontoons being slightly

higher from the close proximity of the pontoons, which allows the ramp to make contact at a lower angle.

In comparison to other proposed discrete and continuous excavation systems, it was found that CASPER was not a superior technology due to the inefficiencies incurred by using screws as a mobility system. At the same time, it shows promise as an excavator due to the fact that its specific excavation rate is higher than most of the examined systems, and nearly as high as the top performers. According to the ETR data, CASPER is approximately a factor of 3-4 less effective than all of the continuous and discrete excavation systems it was compared with, except for the backhoe excavation system. However, these results are promising for a first-generation prototype that is dramatically less massive than all other systems, and further development and investigation into this system architecture is warranted.

5.2   Future Research

Throughout the design, testing, and analysis of the CASPER prototype, many promising avenues of future work have been identified. First and foremost, increasing the scale of CASPER and operating it in a field environment, or a more versatile lab environment with more accurate analogues of lunar or Martian regolith would be extremely enlightening in determining if the CASPER architecture would be a worthwhile candidate for extra-terrestrial ISRU and terrestrial excavation applications. One major avenue of upgrading CASPER's capability would be adding a navigation system in order to precisely control the direction of travel and correct for any deviations due to the lateral forces induced by the excavation ramp. Additionally, the next version of CASPER would ideally have an on-board power system to eliminate the

need for tethering and to enable field tests. Also, incorporating computer vision to identify rocks or other obstacles would enable a future version of CASPER to avoid hazards and investigate how obstacle avoidance impacts excavation performance. Furthermore, adding a system to measure the excavated mass in real time would enable an investigation on how the dynamics and mobility performance of the craft is impacted as it takes on mass. Ultimately, this investigation has shown a great deal of promise for discrete scooper excavation systems, and has shown that Archimedes screw propulsion systems can substantially augment the excavation capabilities of discrete excavation systems.

REFERENCES

[1] *Apollo Lunar Roving Vehicle*. NASA Goddard Space Flight Center, 2016. URL: https://nssdc.gsfc.nasa.gov/planetary/lunar/apollo_lrv.html.

[2] Nicholas C Costes, John E Farmer, and Edwin B George. *Mobility Performance of the Lunar Roving Vehicle: Terrestrial Studies, Apollo 15 Results*. Vol. 401. NASA, 1972.

[3] Vivake Asnani, Damon Delap, and Colin Creager. 'The development of wheels for the Lunar Roving Vehicle'. In: *Journal of Terramechanics* 46.3 (2009), pp. 89–103.

[4] Saverio F Morea. 'The lunar roving vehicle: Historical perspective'. In: *Lunar Bases and Space Activities of the 21st Century*. 1992.

[5] *Three Generations of Rovers in Mars Yard*. NASA. URL: https://mars.nasa.gov/resources/3792/three-generations-of-rovers-in-mars-yard/.

[6] *Rover Wheel Sizes (Isometric)*. NASA/Caltech, 2007. URL: https://www.jpl.nasa.gov/images/rover-wheel-sizes-isometric.

[7] Brian Wilcox and Tam Nguyen. *Sojourner on mars and lessons learned for future planetary rovers*. Tech. rep. SAE Technical Paper, 1998.

[8] Wesley B Williams and Eric J Schaus. 'Design and Implementation of a Rocker-Bogie Suspension for a Mining Robot'. In: *ASEE Southeast Section Conference*. 2015.

[9] Randel A Lindemann and Chris J Voorhees. 'Mars Exploration Rover mobility assembly design, test and performance'. In: *2005 IEEE International Conference on Systems, Man and Cybernetics*. Vol. 1. IEEE. 2005, pp. 450–455.

[10] Scott Moreland et al. 'Soil behavior of wheels with grousers for planetary rovers'. In: *2012 IEEE Aerospace Conference*. IEEE. 2012, pp. 1–8.

[11] Scott Jared Moreland. 'Traction processes of wheels on loose, granular soil'. PhD thesis. Doctoral Dissertation, Carnegie Mellon University, 2013.

[12] Ravi Prakash et al. 'Mars Science Laboratory entry, descent, and landing system overview'. In: *2008 IEEE Aerospace Conference*. IEEE. 2008, pp. 1–18.

[13] S Haggart and J Waydo. 'The mobility system wheel design for NASA's Mars Science Laboratory Mission'. In: *11th European Conference of the International Society for Terrain-Vehicle Systems, Torino, Italy.* 2008.

[14] Xiangwu Zeng et al. 'Calculation of excavation force for ISRU on lunar surface'. In: *45th AIAA aerospace sciences meeting and exhibit.* 2007, p. 1474.

[15] Allen Wilkinson and Alfred DeGennaro. 'Digging and pushing lunar regolith: Classical soil mechanics and the forces needed for excavation and traction'. In: *Journal of Terramechanics* 44.2 (2007), pp. 133–152.

[16] GH Just et al. 'Parametric review of existing regolith excavation techniques for lunar In Situ Resource Utilisation (ISRU) and recommendations for future excavation experiments'. In: *Planetary and Space Science* 180 (2020), p. 104746.

[17] Freyr Hardarson. *Locomotion for difficult terrain.* Citeseer, 1998.

[18] Lawrence C Greer et al. *Cratos: The Evolution of a Robotic Vehicle.* Tech. rep. NASA/TM-2013-216491, 2013.

[19] John Caruso et al. 'Cratos: A Simple Low Power Excavation and Hauling System for Lunar Oxygen Production and General Excavation Tasks'. In: *PTMSS Conference.* 2013.

[20] Krzysztof Skonieczny et al. 'Advantageous bucket-wheel configuration for lightweight planetary excavators'. In: (2011).

[21] Robert P Mueller et al. 'Regolith advanced surface systems operations robot (RASSOR)'. In: *2013 IEEE Aerospace Conference.* IEEE. 2013, pp. 1–12.

[22] Linda Herridge and Kim Shiflett. 'Help NASA Design a Robot to Dig on the Moon'. In: *NASA.gov* (). URL: https://www.nasa.gov/feature/help-nasa-design-a-robot-to-dig-on-the-moon.

[23] Krzysztof Skonieczny, DS Wettergreen, and WL "Red" Whittaker. 'Advantages of continuous excavation in lightweight planetary robotic operations'. In: *The International Journal of Robotics Research* 35.9 (2016), pp. 1121–1139.

[24] Krzysztof Skonieczny, Thomas Carlone, David S Wettergreen, et al. 'Considering the effects of gravity when developing and field testing planetary excavator robots'. In: *Field and Service Robotics.* Springer. 2016, pp. 299–312.

[25] David Wettergreen et al. 'Design and field experimentation of a prototype lunar prospector'. In: *The International Journal of Robotics Research* 29.12 (2010), pp. 1550–1564.

[26] MJ Neumeyer and BD Jones. 'The marsh screw amphibian'. In: *Journal of Terramechanics* 2.4 (1965), pp. 83–88.

[27] Ken Evans. 'The history, challenges, and new developments in the management and use of bauxite residue'. In: *Journal of Sustainable Metallurgy* 2.4 (2016), pp. 316–331.

[28] Liang Ju et al. 'Experimental results of a novel amphibian solution for aquatic robot'. In: *2010 IEEE International Conference on Robotics and Automation*. IEEE. 2010, pp. 2261–2266.

[29] *The training of the search and rescue detachment of the Central Military District to detect and evacuate the crew of the Soyuz TMA spacecraft (Chela region)*. Russian Ministry of Defense, 2017. URL: http://xn--80ahclcogc6ci4h.xn--90anlf bebar6i.xn--p1ai/multimedia/photo/gallery.htm?id=36243@cmsPhotoGallery.

[30] Andrew Thoesen, Sierra Ramirez, and Hamid Marvi. 'Screw-generated forces in granular media: Experimental, computational, and analytical comparison'. In: *AIChE Journal* 65.3 (2019), pp. 894–903.

[31] Andrew Thoesen, Sierra Ramirez, and Hamid Marvi. 'Screw-powered propulsion in granular media: An experimental and computational study'. In: *2018 IEEE International Conference on Robotics and Automation (ICRA)*. IEEE. 2018, pp. 4283–4288.

[32] Andrew Thoesen et al. 'Revisiting scaling laws for robotic mobility in granular media'. In: *IEEE Robotics and Automation Letters* 5.2 (2020), pp. 1319–1325.

[33] Andrew Thoesen et al. 'Comparative performance of granular scaling laws for lightweight grouser wheels in sand and lunar simulant'. In: *Powder Technology* 373 (2020), pp. 336–346.

[34] Andrew Thoesen, Teresa McBryan, and Hamidreza Marvi. 'Helically-driven granular mobility and gravity-variant scaling relations'. In: *RSC advances* 9.22 (2019), pp. 12572–12579.

[35] Andrew Thoesen et al. 'Granular scaling laws for helically driven dynamics'. In: *Physical Review E* 102.3 (2020), p. 032902.

[36] Norman S Nise. *Control systems engineering*. John Wiley & Sons, 2020.

[37] V. Nardelli et al. 'An experimental investigation of the micromechanics of Eglin sand'. In: *Powder Technology* 312 (2017), pp. 166–174. DOI: https://doi.org/10.1016/j.powtec.2017.02.009. URL: https://www.sciencedirect.com/science/article/pii/S0032591017301262.

[38] Huiyang Luo et al. 'Effect of mass density on the compressive behavior of dry sand under confinement at high strain rates'. In: *Experimental mechanics* 51.9 (2011), pp. 1499–1510.

[39] 'Commercial Grade Sands: Material Data Safety Sheet'. In: Quikrete Cement and Concrete Products. 2010.

[40] Matt Heverly et al. 'Traverse performance characterization for the Mars Science Laboratory rover'. In: *Journal of Field Robotics* 30.6 (2013), pp. 835–846.

[41] Vidu Jayanetti. 'Basilisk Lizard Inspired Methods for Locomotion on Granular and Aquatic Media with Robotic Applications'. MA thesis. Arizona State University, 2018.

[42] John Caruso et al. 'Excavation on the moon: Regolith collection for oxygen production and outpost site preparation'. In: *46th AIAA Aerospace Sciences Meeting and Exhibit*. 2008, p. 808.

[43] Paul J van Susante and Chris B Dreyer. 'Lunar and planetary excavation prototype development and testing at the colorado school of mines'. In: *Earth and Space 2010: Engineering, Science, Construction, and Operations in Challenging Environments*. 2010, pp. 1191–1200.